Diamictitic iron formation (DIF) deposits of the Neoproterozoic Nova Aurora Iron District (Macaúbas Group, Southeast Brazil)

Francisco Teixeira Vilela [a,b,*], Antonio Pedrosa-Soares [a,1], Marly Babinski [c,1], Cristiano Lana [e,1], Ricardo I.F. Trindade [f,1], Eduardo Santos [d]

[a] Universidade Federal de Minas Gerais, Programa de Pós-Graduação em Geologia, IGC-CPMTC, Campus Pampulha, Av. Antônio Carlos 6627, Belo Horizonte, 31270-901, MG, Brazil
[b] Geological Survey of Brazil – CPRM, Av. Brasil 1731, Belo Horizonte, 30140-003, MG, Brazil
[c] Universidade de São Paulo, Centro de Pesquisas Geocronológicas, Instituto de Geociências, Rua do Lago 562, São Paulo, 05508-080, SP, Brazil
[d] Sul Americana de Metais S/A – SAM, Av. Contorno 5919, Belo Horizonte, 30110-927, MG, Brazil
[e] Universidade Federal de Ouro Preto, DEGEO, Laboratório de Geoquímica Isotópica, Ouro Preto, Brazil
[f] Universidade de São Paulo, Instituto de Astronomia, Geofísica e Ciências Atmosféricas, Departamento de Geofísica, São Paulo, 05508-090, SP, Brazil

ARTICLE INFO

ABSTRACT

The best-known Neoproterozoic glaciation-related iron deposits are the Rapitan-type banded iron formation (BIF) formed dominantly by chemical-sedimentary processes. We present a detailed study on a distinct type of glaciation-related iron deposit: the iron-rich metadiamictites of the Nova Aurora Iron District, comprising over 20 billion tons of iron oxide-rich rocks: the diamictitic iron formations (DIF >15 wt% Fe) and ferruginous metadiamictites (FD: 5–15 wt% Fe). Drill core logging, field mapping and analytical data revealed the protoliths, sediment sources, depositional environment, and ore enrichment processes on the iron district, and were used to discuss differences between the studied DIF and classic Rapitan-type BIF. U–Pb age spectra and Lu–Hf data for detrital zircon grains revealed a wide range of sediment sources and a maximum depositional age around 879 Ma. These data support correlations of the Nova Aurora iron deposits with the Cryogenian Macaúbas rift, a basin filled by glaciomarine successions related to the Sturtian glaciation event. The matrices of prevailing hematite-rich metadiamictites comprise (in vol %): hematite (7–55), quartz (17–57), muscovite (2–40), carbonate (<1–30), biotite (<1–18), chlorite (<1–23), epidote (<1–7), magnetite (1–5), and traces of tourmaline (<3), apatite (<3) and zircon (<1), with hematite, mica and stretched quartz outlining the metamorphic foliation. Clasts are free of iron-rich rocks. Hematite reconcentration (>50 wt% Fe) occurs in local mylonitic shear zones and tightly crenulated bands after gangue minerals removal during deformation. Late hydrothermal alteration formed magnetite-rich metadiamictite in high-strain zones. From base to top, the stratigraphic type-section of the Nova Aurora Iron District shows barren metadiamictite with quartz-rich matrix and graded-bedded quartzite lenses, followed by hematite-rich-matrix metadiamictite, then passing to muscovite-rich-matrix metadiamictite gradually richer in magnetite and sulfide, enclosing metapelite lenses. This section presents a fining-up graded-bedded succession with clasts size decreasing upwards and recurrent load structures, typical of debris flows and turbiditic sedimentation. The hematite/mica, Fe/Al, Fe/Ti and Fe/REE ratios, as well as the biotite/muscovite and silicate/sulfide ratios, which accompany variations in the oxidizing conditions, decrease to the top. Accordingly, the early protoliths were quartz-rich diamictites that passed to iron-rich diamictites and then to clay-rich, and under more reducing conditions, sulfide-bearing diamictites. Sedimentological and geochemical evidences suggest ferrous-iron accumulation followed by iron oxide precipitation from seawater when the conditions changed from anoxic to oxidizing by the input of oxygen-rich waters from deglaciation, followed by increasing reducing conditions accompanying marine transgression. These processes took place in a relatively restricted sector of the glaciomarine basin, probably a graben of the Cryogenian Macaúbas rift. Differences in relation to the classic Rapitan-type iron formations are the coarse-grained (rudic) texture and the massive

---

* Corresponding author. Universidade Federal de Minas Gerais, Programa de Pós-Graduação em Geologia, IGC-CPMTC, Campus Pampulha, Av. Antônio Carlos 6627, Belo Horizonte, 31270-901, MG, Brazil.
E-mail address: francisco.vilela@cprm.gov.br (F.T. Vilela).
[1] Fellow of the Brazilian Council for Science and Technology Development (CNPq).

structure, the high-energy sedimentary environment, and the absence of true BIF in the Nova Aurora DIF deposits.

1. Introduction

Iron formations (IF) stand out for their unique economic role, and great importance to understand the atmosphere and hydrosphere evolution (e.g., Bekker et al., 2010, 2014; Cox et al., 2013, 2016). Several approaches have been applied to classify the different IF types, including mineralogical composition (oxide facies, carbonate facies, silicate facies and sulfide facies; James, 1954), depositional environments (Algoma-type and Lake Superior-type; Gross, 1980), lithological subtypes (banded IF and granular IF; Trendall, 2002) and, according to a broader perspective, proximity of hydrothermal vents or deposition on continental shelves (Bekker et al., 2010, 2012).

Although scattered in the geological record, iron formations are only widespread in Archean to Siderian terranes (Trendall, 2002; Bekker et al., 2010; Klein, 2005). Late Paleoproterozoic and Mesoproterozoic iron formations generally form small occurrences and only a few voluminous deposits are known (Bekker et al., 2010, 2014; Canfield et al., 2018; Rolim et al., 2016; Silveira-Braga et al., 2015; Barrote et al., 2017; Rosière et al., 2019). The largest Neoproterozoic deposits comprise Rapitan-type banded iron formation (BIF) and other iron-rich rocks associated with Cryogenian glaciations (Table 1) (Urban et al., 1992; Klein and Beukes, 1993; Klein, 2005; Piacentini et al., 2007; Cox et al., 2013, 2016). Table 1 presents the main features of selected deposits of Neoproterozoic iron formations.

Classic Rapitan-type deposits comprise hematitic jaspillite, hematitic siltstone and massive diamictite with hematite–jasper matrix, like those of the Rapitan Group (NW Canada) with an iron ore reserve over 18 billion tons (Young, 1976; Klein and Beukes, 1993; Halverson et al., 2011; Baldwin et al., 2012; Cox et al., 2016). Other examples of glaciation-related Neoproterozoic IF deposits are found in the Damara, Gariep and Otavi belts of South Africa and Namibia (Lechte and Wallace, 2016; Smith, 2018; Lechte et al., 2018b), the Braemar ironstone facies of the Umberatana Group in South Australia (Lottermoser and Ashley, 2000; Lechte and Wallace, 2016), the Urucum District of central-western Brazil (Klein and Ladeira, 2004; Piacentini et al., 2007; Angerer et al., 2016), the Yerbal Formation of the Arroyo del Soldado Group, Uruguay (Pecoits et al., 2008), the Fulu Formation of the Jiangkou Group, South China (Zhang et al., 2008; Feng et al., 2017; Busigny et al., 2018) and the Kingstone Peak Formation, California, USA (Lechte et al., 2018a, Table 1).

Although most Neoproterozoic IF are associated with the Cryogenian (720-635 Ma) glaciations (Klein and Beukes, 1993, Lottermoser and Ashley, 2000; Cox et al., 2013, 2016, Baldwin et al., 2012; Halverson et al., 2011), there are iron-rich Neoproterozoic deposits lacking glaciation-related features, either similar to continental shelf deposits (Lake Superior-type) such as those from the Dahongliutan iron formations (Hu et al., 2020, Table 1) or related to volcanism, like those found in the Arabian-Nubian Shield (Basta et al., 2011; Gaucher et al., 2015; El-Rahman et al., 2019, Table 1). Genesis of Neoproterozoic IF has been addressed in several models (e.g., Cox et al., 2013), seeking to clarify the iron source, as well as the iron deposition mechanism and chemical conditions. Several iron sources have been suggested, like the input of hydrothermal fluids in the basin (Breitkopf, 1988; Young, 1988), ocean-floor leaching by low-temperature hydrothermal fluids (Halverson et al., 2011), iron input by anoxic sub-glacial outwash (Cox et al., 2013) and iron supply from the continent (Swanson-Hysell et al., 2010). Iron concentration in marine basins can be related to anoxic conditions imposed by global ice covers (cf. the Snowball Earth hypothesis; Kirschvink, 1992; Hoffman et al., 1998) or to local ice covers in restricted basins (Baldwin et al., 2012). Iron deposition can be explained by oxidation related to basin-atmosphere interactions at the end of the glaciation (Kirschvink, 1992) and/or by mixing processes between deep ferruginous waters with shallow oxygenated waters (Halverson et al., 2011) or yet by the supply of oxygenated fluids of glacial origin (Lechte et al., 2018a).

Since the early 20th century, glaciation-related features have been reported from the Macaúbas Group of Southeast Brazil (cf. synthesis in Pedrosa-Soares et al., 2011a). In northern Macaúbas Group (Minas Gerais State), voluminous deposits of iron-rich metadiamictites are known since the early 1970's (Velasco and Costa, 1970; Schobbenhaus, 1972). They make up the Nova Aurora Iron District (Fig. 1) comprising over 20 billion tons of diamictitic iron formation (DIF >15 wt% Fe) and ferruginous metadiamictites (FD: 5–15 wt% Fe), with an average ore grade of 17–35 wt% Fe (Viveiros et al., 1978; Vilela et al., 2014). The units of the Nova Aurora Iron District are extensively covered by thick lateritic soils but surface mapping, borehole drilling and integration data models (Vilela, 2010; Mario, 2015; Voll et al., 2020) confirm the strong magnetic anomalies that track iron-rich metadiamictite deposits for over 150 km, outlining tightly folded layers (Fig. 1D). However, representative sampling sections cutting across the iron-rich metadiamictite section can only be accessed in drilling borehole cores, like those on blocks 7 and 8 here presented (Fig. 1C and D). Therefore, our study is based on logging and sampling of borehole cores, coupled with detailed surface mapping, ore petrography, bulk-rock geochemistry and isotopic (U–Pb, Lu–Hf) zircon analysis. The resulting dataset, combined with compiled data, unravels the sedimentary protoliths of iron-rich metadiamictites and the related depositional environment, as well as the iron enrichment processes imposed by tectonics and metamorphism. We also compare the studied iron-rich metadiamictites with the classic Rapitan-type BIF and other Neoproterozoic iron formations, providing a robust basis to characterize DIF (diamictitic iron formation) deposits elsewhere.

2. Geological setting

The study region (Fig. 1) is located on the western Araçuaí Orogen (Pedrosa-Soares et al., 2001, 2008). It comprises the Porteirinha basement block mostly composed of Archean and Paleoproterozoic orthogneisses and granitic rocks (Silva et al., 2016; Bersan et al., 2018), the Statherian-Stenian Espinhaço Supergroup, a rift-related succession consisting of quartzite and metaconglomerate with minor pelitic and volcanic rocks (Chaves et al., 2013; Costa et al., 2018; Costa and Danderfer, 2017), and the Neoproterozoic Macaúbas Group (Fig. 2A), a metavolcano-sedimentary succession over 10 km thick (Pedrosa-Soares et al., 2011a).

From the base to top (Fig. 2A) and west to east (Fig. 1B and C), the Macaúbas Group includes the diamictite-free Rio Peixe Bravo Formation, deposited in an Early Tonian aulacogen (ca. 950-880 Ma, Rift 1 in Fig. 2), and the Serra do Catuni, Nova Aurora and Chapada Acauã formations, rich in diamictites, representing the glaciogenic infill of a Cryogenian continental rift (ca. 720-670 Ma, Rift 2 in Fig. 2) that evolved to passive margin basin and ocean-floor spreading up to the very early Ediacaran (Pedrosa-Soares et al., 2011a; Babinski et al., 2012; Kuchenbecker et al., 2015; Castro et al., 2019, 2020; Souza et al., 2019; Amaral et al., 2020).

Bordering the eastern edge of the Porteirinha block (Fig. 1C), the Rio Peixe Bravo Formation comprises quartzite, metapelite and rare metaconglomerate lenses, deposited in a fluvial to shallow-marine environment with no glacial evidence (Viveiros et al., 1978; Noce et al., 1997; Pedrosa-Soares et al., 2011a).

Further east, the Nova Aurora Formation, a thick (1–3 km) package of stratified diamictites with lenses of graded sandstone and pelite,

Table 1

Main features of selected deposits of Neoproterozoic iron formations (IF), banded iron formations (BIF) and diamictitic iron formations (DIF). 1, This work; 2, Piacentini et al. (2007); 3, Klein and Ladeira (2004); 4, Angerer et al. (2016); 5, Cox et al. (2013); 6, Lechte and Wallace (2016); 7, Lottermoser and Ashley (2000); 8, Klein and Beukes (1993); 9, Halverson et al. (2011); 10, Busigny et al. (2018); 11, Feng et al. (2017); 12, Lechte et al. (2018a); 13, Ilyin (2009); 14, Basta et al. (2011); 15, El-Rahman et al. (2019); 16, Stern et al. (2013); 17, Hu et al. (2020); 18, Castro et al. (2020); 19, Pedrosa-Soares (1995); 20, Pedrosa-Soares et al. (1998); 21, Queiroga (2010); 22, Amaral et al. (2020); 23, Castro et al. (2019); 24, McGee et al. (2018). Sturtian glaciation age by Rooney et al. (2015). Macaúbas Group I includes the Early Tonian units, and Macaúbas Group II the Cryogenian units (cf. Pedrosa-Soares and Alkmim, 2011; Pedrosa-Soares et al., 2011a; Kuchenbecker et al., 2015; Castro et al., 2019, 2020; Amaral et al., 2020). BIF, DIF and IF: Fe > 15 wt%; ferruginous diamictite (FD): Fe = 5–15 wt %. *age of detrital zircons; #age of metamorphism.

Local name	Location	Stratigraphic unit	Thickness (m)	Average wt% Fe	Resource (10⁹ tons)	Main iron oxides	Main gangue	Main iron-rich rocks	Minor iron-rich rocks	Depositional Environment	Age (Ma)	Correlation to glaciation	Ref.
Nova Aurora Iron District	Minas Gerais, Brazil	Nova Aurora Formation, Macaúbas Group	50–600	25	20	hematite, magnetite	quartz, muscovite, carbonate	hematite-rich DIF and FD	magnetite-rich metadiamictite	high-energy distal glaciomarine, followed by transgression	<854* >570#	Sturtian	1, 18
Urucum Iron–Manganese District	Mato Grosso, Brazil; Eastern Bolivia	Puga and Santa Cruz formations, Jacadigo Group	75–270	44	36	hematite, jasper, magnetite	quartz, muscovite	hematite-rich BIF	centimetric banding BIFs	shallow glaciomarine, associated to transgression	<686* >560#	Marinoan	2, 3, 4.24
Chuos and Numees	Namibia	Chuos Formation	greatly variable	28		magnetite	chert	jaspilite, laminated IF	massive ferruginous diamictites	low-energy, sub–ice shelf, ice-proximal glaciomarine	717–660	Sturtian	5, 6
Oparina, Halowilena and Braemar	South Australia	Braemar Ironstone, Umberatana Group	100	29	4.2	hematite	quartz, muscovite, carbonate	laminated IF	diamictitic ironstone	low-energy, sub–ice shelf, ice-proximal glaciomarine	717–660	Sturtian	5, 6, 7
Rapitan	Northwestern North America	Sayunei Formation, Rapitan Group	20–100	28	18	hematite and jasper	chlorite, smectite, quartz, carbonate	BIF and laminated IF	ferruginous diamictites	low- to high-energy glaciomarine associated to transgression	720	Sturtian	5, 8, 9
Fulu	South China	Fulu Formation	8–50	15		hematite	quartz, biotite, feldspar, chamosite	laminated IF	ferruginous siltstones	low-energy, sub–ice shelf, ice-proximal glaciomarine	716–691	Sturtian	10, 11
Kingstone Peak	California, USA	Kingston Peak Formation, Pahrump Group	<10	29		hematite	detrital clays, chert, chlorite	laminated ferruginous shales		intermediate to ice-distal glaciomarine			12
Mugur	Tuva, Mongolia	Mugur Formation	10	38	0.3	magnetite	quartz	BIF			767–600		13
Wadi and Silasia	Arabian-Nubian Shield	Silasia Formation	10–90	42		magnetite	quartz, carbonate	BIF	island arc		750–696		14, 15, 16
Dahongliutan	Northwestern China	Dahongliutan IF	100	33		hematite	quartz, dolomite, calcite, muscovite	oxide facies BIF	silicate and carbonate facies BIF	shallow shelf	593		17
Ribeirão da Folha Formation	Minas Gerais, Brazil	Macaúbas Group II	<10	30		magnetite	quartz, amphibole	magnetite-rich BIF	silicate and sulfide facies BIF	ophiolite complex	645		19, 20, 21, 22
Capelinha Formation	Minas Gerais, Brazil	Macaúbas Group I	<10	22		magnetite	quartz, mica	oxide-facies BIF	quartzite	continental rift	930		21, 23

metamorphosed in greenschist facies, unconformably overlies the Rio Peixe Bravo Formation (Viveiros et al., 1978; Noce et al., 1997; Uhlein et al., 1999; Pedrosa-Soares et al., 2011a; Vilela et al., 2014).

The Nova Aurora Formation is one of the glaciomarine successions of the Macaúbas Group (Karfunkel and Hoppe, 1988; Pedrosa-Soares et al., 1992, Pedrosa-Soares et al., 2011a; Uhlein et al., 1998, 1999; Castro et al., 2020), comprising massive to poorly stratified diamictites, clast-poor diamictites with clasts size decreasing upwards, and lenses of fining-up graded-bedded sandstones and pelites with load structures.

The Nova Aurora Formation represents mass (debris) flows and high-to-low density turbidites, deposited during the Cryogenian rift stage (Rift 2, Fig. 2) of the Macaúbas basin (Pedrosa-Soares and Alkmim, 2011; Pedrosa-Soares et al., 2011a; Babinski et al., 2012; Kuchenbecker et al., 2015). More recently, detailed sedimentological-stratigraphic studies coupled with robust U–Pb and Lu–Hf data constrained the sedimentation age of Macaúbas glaciomarine deposits between 720 and 670 Ma (Castro et al., 2020), providing solid evidence to support previous correlations with the Sturtian glaciation event (Pedrosa-Soares
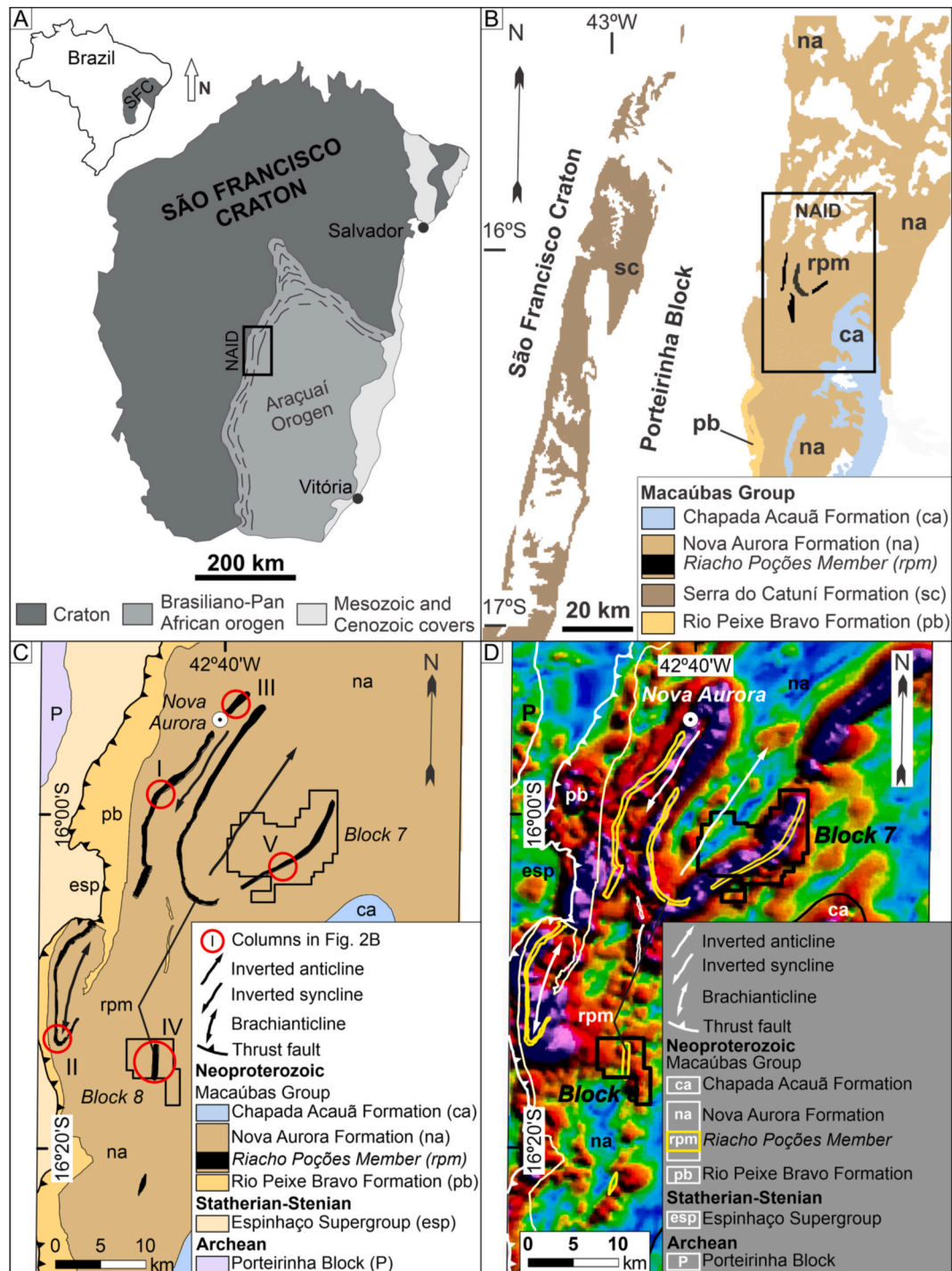

Fig. 1. (A) Regional location of the Nova Aurora Iron District (black polygon) in western Araçuaí Orogen to the east of the São Francisco Craton (SFC), and (B) Simplified regional map covering the Macaúbas Group (both modified from Pedrosa-Soares et al., 2011a); (C) Regional geological map including the Nova Aurora Iron District (modified from Pinto and Silva, 2014, and Lombello, 2020); (D) Image for the Total Gradient Amplitude (TGA) from airborne magnetic survey (data from CODEMIG-SEDE-CPRM (2006).

et al., 2011a; Babinski et al., 2012).

A sub-unit of the Nova Aurora Formation, the Riacho Poções Member, encompasses the iron-rich metadiamictites of the Nova Aurora Iron District (Fig. 2). According to systematic geological mapping, airborne geophysical survey, prospecting work (including more than 220 km of borehole drilling) and data integration modelling, the Nova Aurora Iron District includes iron-rich diamictites composing up to 50 km long segments of the Riacho Poções Member (Viveiros et al., 1978; Vilela, 1986, 2010; Mourão and Grossi-Sad, 1997; Noce et al., 1997; Roque et al., 1997; Pedrosa-Soares et al., 2011a; Vilela et al., 2014; Mario, 2015; Voll et al., 2020). The layers of iron-rich metadiamictites are thicker to the west, with local apparent thickness up to 600 m (Viveiros et al., 1978), becoming gradually thinner towards the east and southeast (Fig. 2B). Hematite is the most abundant and widespread iron oxide in the metadiamictites of the Nova Aurora Iron District, occurring in the iron-rich metadiamictites that gradually pass to barren metadiamictites, both preserved from the regional deformation, and in strongly deformed iron-rich metadiamictites (columns I and IV in Fig. 2B) (cf. Viveiros et al., 1978, Vilela, 2010, Mario, 2015). Magnetite-rich metadiamictites are only found locally and ever associated to fold hinges (Fig. 2B column III) or major shear zones (Fig. 2B column V; see detailed descriptions on the iron-rich units in section 4).

2.1. Tectonics and metamorphism

During regional tectonics and metamorphism, the Nova Aurora iron-rich diamictites evolved to metadiamictites with hematite and/or magnetite recrystallized along ductile foliations and high-strain zones, and locally re-concentrated by late tectonic hydrothermal processes associated to the shear zones. The regional tectonics and metamorphism (ca. 570–540 Ma) generated distinct sets of tectonic structures related to three deformational phases on the Macaúbas Group (Pedrosa-Soares et al., 1992; Mourão and Grossi-Sad, 1997; Roque et al., 1997; Uhlein et al., 1998; Marshak et al., 2006; Vilela, 2010; Peixoto et al., 2018a).

The first deformation phase (D_1) corresponds to the main regional ductile deformation, characterized by NNE-trending foliation (S_1) dipping 15° to 50° to ESE. Generally, the S_1 foliation is a penetrative schistosity, materialized by oriented mica, hematite and stretched quartz, parallel to the axial plane of west-verging, asymmetric tight to isoclinal folds (F_1) usually partially to completely transposed along fold hinges. A striking stretching lineation (L_1) is marked by elongated, symmetric to sigmoidal clasts in metadiamictites that are parallel to the mineral lineation of mica, hematite and stretched quartz imprinted in the S_1 foliation. Kinematic indicators related to D_1 structures indicate tectonic transport to west, whilst metamorphic mineral assemblages syn-kinematic to S_1 foliation disclose increasing P–T conditions from west to east, reaching the garnet zone of the greenschist facies in the study area (Mourão and Grossi-Sad, 1997; Vilela, 2010; Pedrosa-Soares et al., 2011a, 2011b; Peixoto et al., 2018b).

The second deformation phase (D_2) is characterized by W-dipping (~45°), NS-trending S_2 crenulation cleavage-to-schistosity, crosscutting the S_1 schistosity. The east-verging S_2 cleavage-to-schistosity is parallel to the axial plane of asymmetric cascade folds that refold F_1 tight folds (Alkmim et al., 2006; Marshak et al., 2006). At the latest D_2 stage, normal faults parallel to S_2 show hanging-wall blocks displaced downdip towards east (Marshak et al., 2006). Mica, hematite and quartz recrystallized along S_2 crenulation domains and shear zones, record a low-grade greenschist facies free of garnet (Vilela, 2010; Peixoto et al., 2018a).

Structures related to these two deformation phases can be recognized at various scales, such as the F_1 folds seen in regional geological and geophysical maps (Fig. 1C and D) and the relationships between S_1 and S_2 in outcrops and thin sections, detailed in the following descriptions (Fig. 3 to Fig. 9).

The third deformation phase (D_3) comprises regional brittle deformation, characterized by NW- and NE-trending, conjugated, spaced-fracture systems, associated with large open folds and displacements of large ore blocks (Mourão and Grossi-Sad, 1997; Roque et al., 1997; Vilela, 2010).
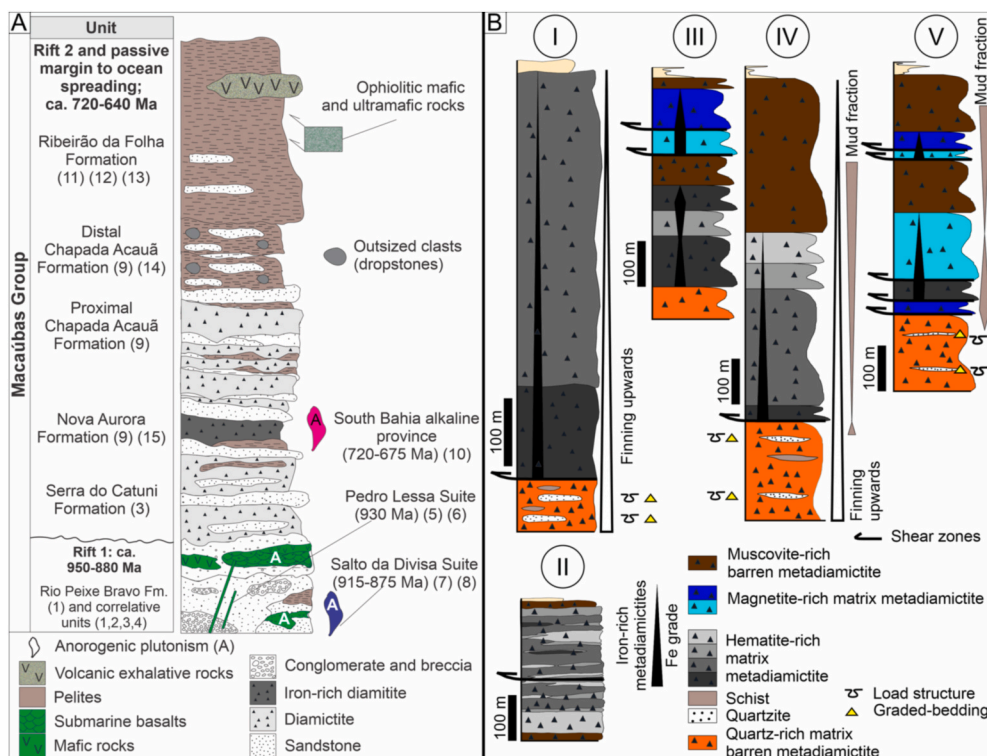

Fig. 2. A) Stratigraphic columns of the Macaúbas Group (modified from Alkmim et al., 2006; Pedrosa–Soares et al., 2008, Pedrosa-Soares et al., 2011a; Pedrosa-Soares and Alkmim, 2011; Castro et al., 2019; Castro et al., 2020). As rocks underwent low-grade metamorphism, we refer to their protoliths. (1) Castro et al. (2019); (2) Souza et al. (2019); (3) Babinski et al. (2012); (4) Souza (2016); (5) Machado et al. (1989); (6) Queiroga et al. (2012); (7) Silva et al. (2008); (8) Menezes et al. (2012); (9) Kuchenbecker et al. (2015); (10) Rosa et al. (2007); (11) Queiroga et al. (2007); (12) Peixoto et al. (2015); (13) Amaral et al. (2020); (14) Castro et al. (2020); (15) This work. B) Typical stratigraphic columns for distinct sections of the Nova Aurora Iron District (see Fig. 1C to column location; see text for complementary references).
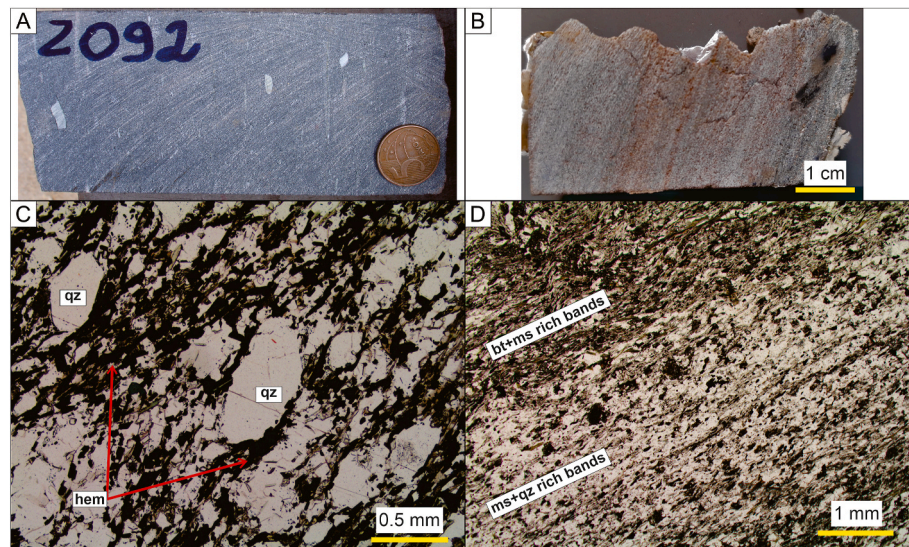
Fig. 3. Photos of samples from drill cores. A) hematite-rich metadiamictite MRP1; B) biotite-muscovite-quartz schist Geocron-1 and respective thin sections under plane-polarized transmitted light; C) sample MRP1; D) sample Geocron-1.

3. Materials and methods

3.1. Lithogeochemistry

Bulk-rock lithogeochemical analyzes were performed on the matrices of 66 metadiamictite samples selected from drill cores (9 barren metadiamictites, 44 hematite-rich ferruginous metadiamictites and 13 magnetite-rich ferruginous metadiamictites), after removing clasts, weathering rust and coats, fracture fillings, and quartz and carbonate veins.

The analyses were performed by the Acme Analytical Laboratories (Vancouver, Canada) and SGS-Geosol Laboratories (Vespasiano, Brazil). Iron contents are referred to as $Fe_2O_{3(t)}$ (total iron). Complete data are available in the Supplementary data A. At SGS-Geosol Laboratories, the samples were only analyzed for their major element oxides (Al_2O_3, CaO, K_2O, MgO, MnO, Na_2O, P_2O_5, Fe_2O_3, SiO_2, and TiO_2) by X-Ray fluorescence after lithium tetraborate melting. Total abundances of the major oxides and several minor elements analyzed at the Acme Analytical Laboratories are reported for 0.1 g of analyzed sample by ICP-AES after lithium metaborate and tetraborate melting and diluted in nitric acid solution. Loss on ignition (LOI) was determined by weigh difference after ignition at 1000 °C. Out of these samples, 23 (5 barren metadiamictites, 15 hematite-rich ferruginous metadiamictites and 3 magnetite-rich ferruginous metadiamictites) were analyzed for their Rare Earth Elements (REE) and refractory elements, determined by ICP-MS, after sample melting with lithium metaborate and tetraborate, and nitric acid digestion of 0.1 g for sample. In addition, a separate 0.5 g split was digested in Aqua Regia and analyzed by ICP-MS to report the precious and base metals.

For the REE data (Supplementary data A), depletion or enrichment of the light Rare Earth Elements (LREE) in relation to the heavy Rare Earth Elements (HREE) are expressed as a $Pr_{(SN)}/Yb_{(SN)}$ (SN: shale-normalized to PAAS – Post-Archean Australian Shale, cf. Taylor and McLennan, 1985). Europium and cerium anomalies were calculated according to Bau and Dulski (1996) as follows:

$$Ce / Ce * = Ce(SN)/(0.5La(SN) + 0.5Pr(SN))$$

$$Eu / Eu * = Eu(SN)/(0.66Sm(SN) + 0.33Tb(SN))$$

Praseodymium anomalies were calculated according to the following equation, and used to identify true or false cerium anomalies (Fig. 13):

$$Pr/Pr * = Pr(SN)/(0.5Ce(SN) + 0.5Nd(SN))$$

3.2. U–Pb geochronology and Lu–Hf isotopic analysis

For U–Pb and Lu–Hf isotopic analyses on detrital zircon grains, two samples were collected from drill cores (Fig. 3), aiming to investigate sediment provenance and maximum depositional age of the iron-rich metadiamictite package. After rock crushing, milling and panning, heavy mineral concentrates were obtained by conventional gravimetric and magnetic (Frantz isodynamic separator) techniques. Zircon grains were then randomly handpicked and mounted in epoxy disks, and polished to expose their centers. Cathodoluminescence (CL) images reveal morphological features and internal structures of zircon grains and were used to select the domains within the zircons for analyses.

The composite sample MRP1 represents specific drill core intervals between 710 and 720 m deep. It comprises only hematite-rich metadiamictite from selected boreholes with well-constrained stratigraphic control (central coordinates in Block 8: 16°14.60′ S, 42°44.25′ W; Figs. 3 and 5). The hematite-rich metadiamictite has a dark to light grey matrix rich in specularite, mainly enclosing clasts of quartzite (Fig. 3A and C). Sample MRP1 was prepared and analyzed at the Geochronological Research Center (CPGeo), University of São Paulo, Brazil. For MRP1 sample, U–Pb and $^{176}Lu/^{177}Hf$ analyzes were carried out using a Neptune MC-LA-ICP-MS coupled to an Excimer ArF ($\lambda = 193$ nm) Laser Ablation. A total of 78 zircon grains from sample MRP1 were analyzed.

The sample Geocron-1 is composed of biotite-muscovite-quartz schist (Fig. 3B and D) and covers about 1 m at around the 565 m depth in the drill core FSF-340, also in Block 8 (coordinates 16°13.40′ S and 42°43.27′ W, Fig. 5). It was collected in the upper transition zone from iron-rich to barren metadiamictites in drill core FSF-340 and is relatively poor in hematite. The Geocron-1 mount was analyzed using an Element-2 Thermo Finnigan coupled with a Photon machines 193 nm laser system of the Isotope Geochemistry and Geochronology Laboratory of the Federal University of Ouro Preto, Brazil. A total of 95 zircon grains from sample Geocron-1 were analyzed.

Data evaluation for each analysis took into account the common Pb contents, errors of isotopic ratios, percentages of concordance and Th/U ratios. Only analyses with concordance more than 90% were used for age calculations and plotting in histograms, using the software Isoplot/Ex (Ludwig, 2003). As all ages are older than 800 Ma, the $^{207}Pb/^{206}Pb$ ages were used for plotting in histograms.
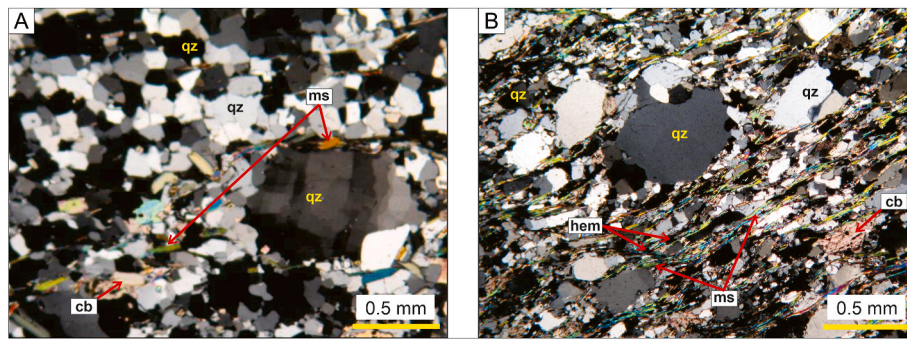
Fig. 4. Photomicrographs of thin sections under plane-polarized transmitted light (qz: quartz; ms: muscovite; cb: carbonate; hem: hematite): A) quartz-rich matrix metadiamictite; B) mica-rich-matrix metadiamictite. Stratigraphic references in Figs. 5 and 6.
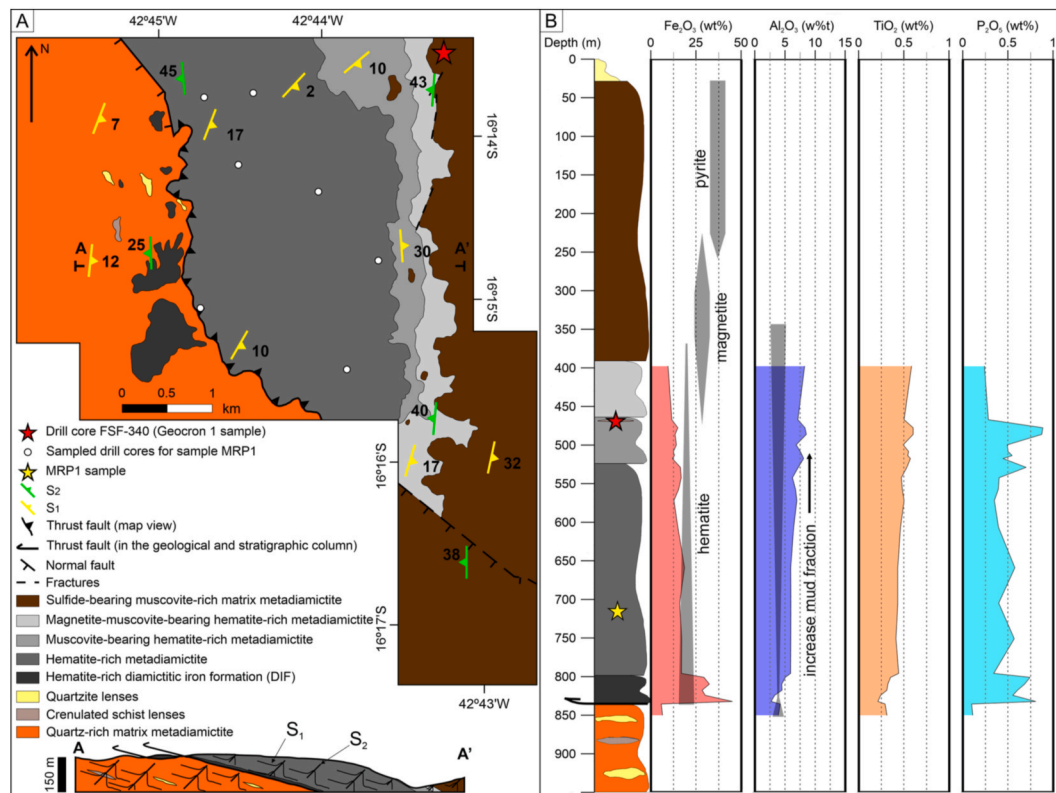

Fig. 5. Geological and geochemical data from surface mapping and drill cores on Block 8 (stars on sampled borehole drill cores): A) Geological map (see also Fig. 1C) and geological cross section A-A'. B) Lithologic and geochemical logs.

Lu–Hf isotopic analyses of zircon were carried out in the same grain domains analyzed for U–Pb dating. The laser was operated with a spot of 47 μm in diameter, fluence of 1.61 J/cm 250 s, and a pulse rate of 7 Hz. The εHf$_{(t)}$ values calculation considered a decay constant for ^{176}Lu of 1.867×10^{-11} (Söderlund et al., 2004) and present-day chondritic ratios of ^{176}Hf/^{177}Hf = 0.282772 and ^{176}Lu/^{177}Hf = 0.0332 (Blichert-Toft and Albarede, 1997). The Hf evolution curve of the depleted mantle was determined from present-day depleted mantle values with ^{176}Hf/^{177}Hf ratio of 0.283225 and ^{176}Lu/^{177}Hf ratio of 0.038512 (Vervoot and Blichert-Toft, 1999). The analyzes were done in the same laboratories as the respective U–Pb analyses were made.

4. Iron-rich metadiamictite deposits

The Nova Aurora Iron District (Fig. 1C) comprises layers and lenses of iron-rich metadiamictites enclosed by barren metadiamictites (Fe < 5 wt%) in the Riacho Poções Member at the lower Nova Aurora Formation

(Macaúbas Group; Figs. 2, 5 and 6).

The Nova Aurora Iron District comprises distinct iron-rich metadiamictites, concerning the iron content and prevail ore mineral (Fig. 2B, Table 2). The diamictitic iron formations (DIF) contain total Fe > 15 wt% (or total iron as Fe$_2$O$_{3(t)}$ > 21.45 wt%), including hematite-rich DIF and magnetite-rich DIF. Barren metadiamictites have less than 5 wt% Fe. Hematite-rich and magnetite-rich (or ferruginous) metadiamictites are intermediate members between DIFs and barren metadiamictites (Table 2). Hematite largely prevails in most iron-rich metadiamictites, whereas magnetite is more abundant in ductile shear zones (Figs. 2B and 6).

4.1. Barren metadiamictites (total Fe < 5%)

The barren metadiamictites encompass the regional metadiamictites, including layers and lenses of sulfide-bearing metadiamictite (Figs. 2B, 7B and 8B; Table 2). They show foliated matrix, composed of (vol %,
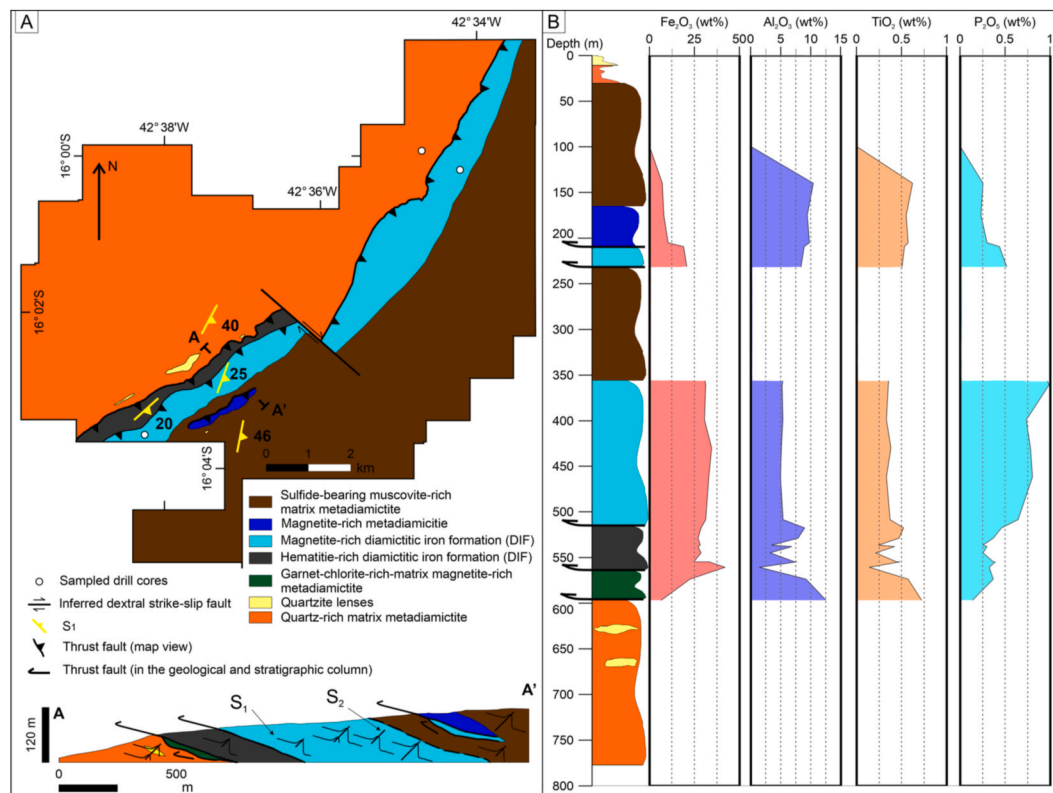
Fig. 6. A) Geological map of Block 7 (location in Fig. 1C) and geological cross section A-A'; B) Stratigraphic column for Block 7, and corresponding geochemical logs for drill cores.

Table 2
Metadiamictites of the Nova Aurora Iron District, according to iron contents (Fe*, total iron, and Fe**, on average iron, contents in wt%) and prevailing iron oxide mineral in rock matrix (in vol%). DIF, diamictitic iron formation. FD, iron-rich or ferruginous metadiamictite. BM, barren metadiamictite. SM, sulfide-bearing metadiamictite. LA, number of lithogeochemical analysis (data are in the Supplementary data A). TS, number of thin sections. Modal contents (in vol%) of minerals estimated from microscopic evaluations under reflected light: Hem, hematite; Mag: magnetite; Qz, quartz; Ms, muscovite; Cb, carbonate; Bt, biotite; Chl, chlorite; Ep, epidote; Ap, apatite; Tur, tourmaline; Py, pyrite; Grt, garnet).

Rock	Fe*	Fe**	LA	TS	Hem	Mag	Qz	Ms	Cb	Bt	Chl	Ep	Ap	Tur	Py	Grt
Hematite-rich DIF	>15	25	13	55	22–55	<1-5	17–57	2–32	<1-30	<1-13	<1-7	<1-7	<1-3	<1-3	<1	–
Magnetite-rich DIF	>15	20	17	15	<1-10	21–40	15–60	2–27	<1-32	<1-21	<1-33	<1	<1	<1-5	<1	<1
Hematite-rich FD	5–15	10	24	48	7–21	1–5	28–57	8–40	<1-33	<1-18	<1-20	<1-7	<1-2	<1-3	–	–
Magnetite-rich FD	5–15	9	4	9	3–10	7–20	40–75	<1-25	<1-45	<1-2	<1-23	<1	<1	<1	<1	<2
BM and SM	<5	3	8	44	1–7	1–5	27–80	5–44	1–48	<1-45	<1-39	<1-10	<1	<1-3	<1-6	<1-17

Table 2) quartz (27–80), muscovite (5–44), biotite (<1–45), chlorite (<1–39), carbonate (<1–48), feldspars (<1), epidote (<1–10), tourmaline (<1–3), apatite (<1), sulfide (<1–6) and zircon (<1). Oriented mica flakes and needles of metamorphic tourmaline, and elongated grains of quartz, carbonate and epidote outline the regional ductile foliation (S_1) and a mineral lineation (L_1) parallel to stretched rock clasts. Rounded-shaped minerals (e.g., carbonate, feldspar, quartz, apatite, tourmaline, and zircon) and rock clasts attest detrital sedimentary provenance. Mica and chlorite outline the S_2 foliation in crenulation domains, crosscutting the S_1 foliation. Locally, barren metadiamictites contain pyrite (up to 6 vol%) and traces of pyrrhotite and chalcopyrite, disseminated in the matrix and stretched along the S_1 foliation, associated with magnetite (<5 vol %) and garnet porphyroblasts (very rarely as much as 17 vol%), characterizing the sulfide-bearing metadiamictites. Mica and garnet contents show positive correlations against quartz, reflecting the increase of alumina content (i.e., in argillaceous mud) in the metadiamictite matrix. Generally, barren metadiamictites rich in muscovite with disseminated sulfide (<6 vol %) overlie iron-rich metadiamictites (Fig. 4). Rarely, barren metadiamictites enclose thin lenses of chlorite schist stretched along the S_1

foliation, which may also contain deformed pyrite crystals.

The barren metadiamictites are polymictic with pebbles to boulders composed of carbonate rock, quartz vein, quartzite, phyllite, micaschist, gneiss, migmatite and granite. Clasts of metapelites and carbonate are usually strongly stretched along the regional lineation (L_1; Fig. 7), whereas larger clasts of quartz vein, quartzite, gneiss and granite usually preserve angular to rounded shapes. Clast distribution varies from chaotic, in massive metadiamictites, to size-classified in stratified metadiamictites with fining-up graded-bedding metasandstone to metapelite lenses, showing load structures. These rock assemblages and depositional structures have been interpreted as mass (debris) flows to turbiditic sedimentation in the Nova Aurora Formation and other diamictitic units of the Macaúbas Group (Pedrosa-Soares et al., 1992, Pedrosa-Soares et al., 2011a; Uhlein et al., 1998, 1999; Castro et al., 2020). Scattered oversized clasts, enveloped by metasandstone and metapelite interleaved with metadiamictites, suggest dropstones from iceberg discharges (cf., Karfunkel and Hoppe, 1988; Pedrosa-Soares et al., 2011a; Castro et al., 2020). Clasts of iron-rich rocks are absent in the barren and iron-rich metadiamictites.
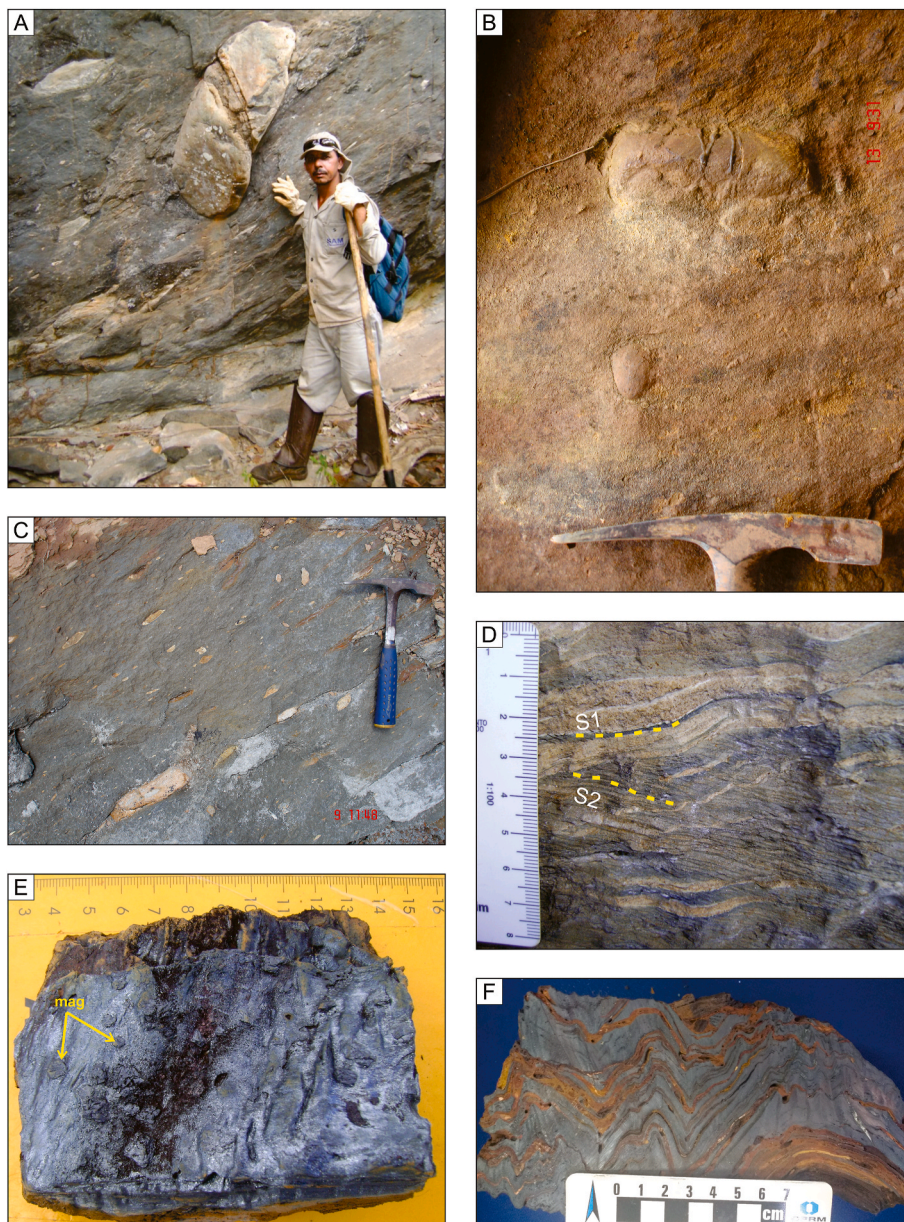
Fig. 7. Metadiamictites of the Nova Aurora Iron District: A) Hematite-rich metadiamictite with outsized clasts (boulders); B) Barren quartz-rich-matrix metadiamictite; C) Stretched clasts parallel to mineral lineation in hematite-rich metadiamictite; D) Hematite-rich metadiamictite with quartzite bands recording primary stratification parallel to the regional schistosity S_1, cut by the S_2 crenulation foliation in hematite-rich layers; E) Crenulated hematite-rich DIF from a basal shear zone (mag: magnetite); and F) Folded and crenulated, banded, hematite-rich DIF with strongly stretched clasts from a basal shear zone.

4.2. Hematite-rich diamictitic iron formation (DIF) and hematite-rich metadiamictite

The most voluminous iron-rich rocks in Nova Aurora deposits are hematite-rich diamictitic iron formation (DIF: Fe > 15 wt%) and hematite-rich metadiamictite (Fe = 5–14 wt%; Table 2; Fig. 2 and Figs. 5–8). In the studied areas, the iron-rich packages range from 50 to 450 m thick (Figs. 5 and 6), and generally show ductile shear zones with striking specularite recrystallization (up to 80 vol%) at the base (Figs. 5B, 6B and 7E, 7F). Along these shear zones, the specularite-rich DIF shows decrease in quartz and other matrix minerals, as well as rotated and stretched rock clasts and magnetite porphyroblasts. Locally, ductile shear zones enriched in magnetite, quartz veins, chlorite and pyrite also outline tectonic contacts between iron-rich metadiamictites and underlying barren metadiamictites (Fig. 8D). The lower sections of the hematite-rich unit show thin layers of quartzite that are barren in iron-oxides (Fig. 7D). The upper layers of iron-rich metadiamictites show metric-thickness lenses of micaschist and scarcity of quartzite intercalations, attesting increase in mud sedimentation against decrease in

sand contribution. Both syn-sedimentary features suggest transition to deeper water environment, probably associated with marine transgression, in relation to the sandy-matrix barren metadiamictites richer in quartzite lenses underlying the iron deposits. Clast assemblages, sizes and compositions are virtually identical in both the hematite-rich metadiamictites and barren metadiamictites. The absence of clasts of iron-rich rocks in both metadiamictites suggests no significant supply of Fe-rich detrital sediments to the basin.

Hematite-rich and metadiamictite and DIF matrices have largely variable modal contents (vol%) of hematite (7–55), quartz (17–57), muscovite (2–40) and carbonate (<1–33), biotite (<1–18), chlorite (<1–20), epidote (<1–7), tourmaline (<3), apatite (<3), and traces of zircon. Hematite content decreases to the top, showing inverse correlation to mica content that increases upwards (Fig. 5). Hematite occurs disseminated and oriented in metadiamictite matrix, forming laminae, bands, and pods along S_1 and S_2 foliations, with reconcentrations at microlithon boundaries (Figs. 7 and 9). Hematite oriented along the S_1 foliation envelops detrital grains, showing no evidence of reaction, replacement, coating and filling of fracture or cleavage on any matrix
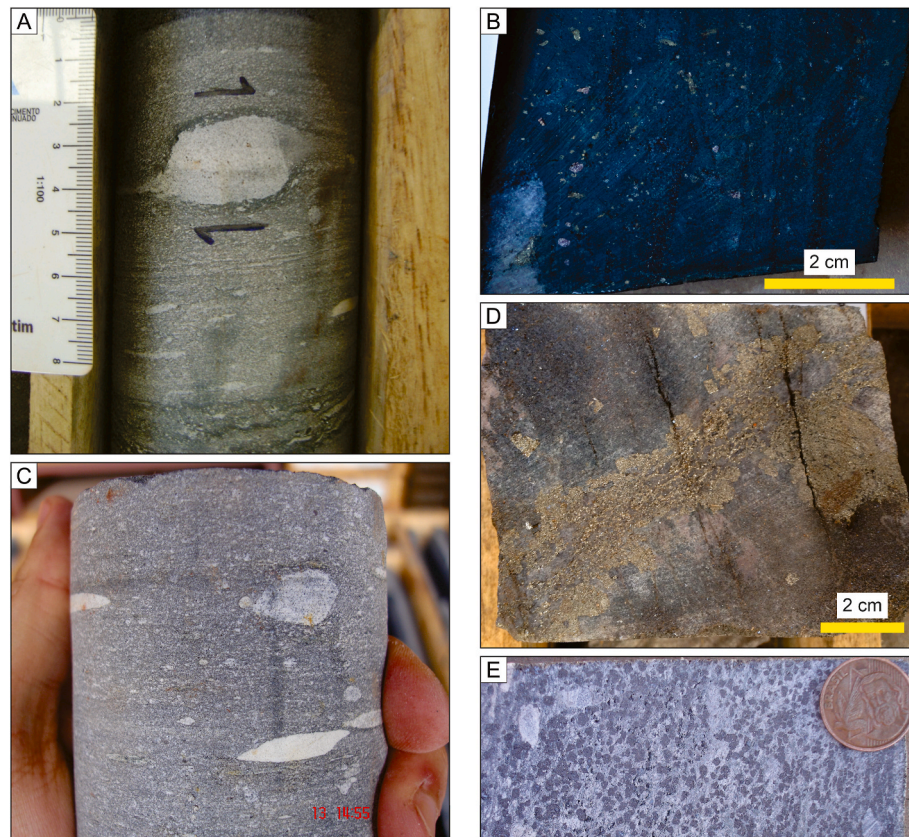
Fig. 8. Core samples from diamond drill holes on the Nova Aurora Iron District. A) Rotated and stretched clasts parallel to S_1 foliation in hematite-rich metadiamictite; B) Sulfide-bearing metadiamictite; C) Hematite-rich metadiamictite from a low-grade iron ore interval; D) Post-S_1 sulfide-rich veinlets and pyrite porphyroblasts in a hematite-rich metadiamictite; E) Diamictitic iron formation (DIF) rich in magnetite porphyroblasts.

components and clasts. Usually forming fine-grained specularite flakes and minute granular crystals (Fig. 9A and B), hematite also may occur as porphyroblasts along S_1 and S_2 foliations (Fig. 9C and D). Fine-grained quartz and carbonate grains are two major components of the matrix and show polygonal recrystallization shapes. Muscovite, biotite, and chlorite, together with hematite, materialize the S_1 foliation, enveloping detrital grains. Partially to fully martitized magnetite porphyroblasts (<5 vol%), commonly deformed with sharp growth edges bounded by quartz, are disseminated in metadiamictite matrix (Fig. 9F). Along high-strain bands, deformed magnetite porphyroclasts display hematite-rich recrystallization tails and pressure shadows filled by quartz and/or carbonate (Figs. 7E and 9E). Apatite is the only phosphorous mineral observed in hundreds of thin sections, showing a clear positive correlation with P_2O_5 content (Figs. 5B and 6B). Tourmaline developed as single prismatic crystals along S_1 foliation and as overgrown rims around rounded cores.

4.3. Magnetite-rich diamictitic iron formation (DIF) and magnetite-rich metadiamictite

Magnetite-rich DIF and magnetite-rich metadiamictite only occur in high-strain ductile shear zones that may reach up to 200 m thick (Figs. 2B and 6), displaying dark-grey bands rich in magnetite alternated with quartz-muscovite-rich bands (Figs. 6 and 8D; Table 2). The greater the magnetite content, the smaller the hematite modal values and darker-colored the metadiamictite. In those rocks, the magnetite (7–40 vol%, Table 2) usually forms undeformed porphyroblasts, disseminated in foliated matrix composed of quartz (15–75 vol%), muscovite (<1–27 vol%), carbonate (<1–45 vol%), biotite (<1–21 vol%), chlorite (<1–33 vol%), hematite (<1–10 vol%), and traces of epidote, apatite, and zircon (Fig. 10). Magnetite shows no evidence of reaction, replacement, coating

and filling features on detrital grains (Fig. 10E and F). In the magnetite-rich metadiamictite, the magnetite is much more abundant than hematite, forming slightly to non-deformed larger crystals than the magnetite of the top transition zone of the iron deposits beneath the upper barren metadiamictite (Fig. 5). Magnetite martitization and specularite recrystallization increase in the highest strain zones (Fig. 10B and D). In the basal shear zone in Block 7 (Fig. 6) there is an increase in chlorite and biotite that may be accompanied by coarse crystals of euhedral garnet porphyroblasts (up to 5 mm in diameter) disseminated in the matrix (<2 vol%) (Fig. 6). These crystals were formed at a late stage, consuming biotite and chlorite and overgrowing the other minerals in the matrix, including magnetite.

5. Analytical results

5.1. Lithogeochemistry

5.1.1. Major elements

The barren metadiamictite matrix rich in quartz has SiO_2 between 68 and 80 wt%, and Fe_2O_3 up to 7% owing to biotite, epidote and pyrite modal contents (Fig. 11A; Supplementary data A). Metadiamictite matrix rich in biotite, chlorite and/or garnet shows abnormally high Fe_2O_3 (up to 20.81 wt%) and Al_2O_3 (up to 12.50 wt%) contents, indicating copious iron-rich mud in the sedimentary protolith. CaO, K_2O and MgO, reaching together 9 wt%, represent feldspar and carbonate clastic fractions.

Matrices of diamictitic iron formation (DIF >15 wt% Fe) and of metadiamictites rich in hematite and/or magnetite (5–15 wt% Fe) have SiO_2 between 13.24 and 78.02 wt% and Al_2O_3 ranging from 0.32 to 12 wt%, reflecting their relatively high contents of quartz, mica and feldspars. Fe_2O_3 content in the hematite-rich metadiamictite matrix ranges
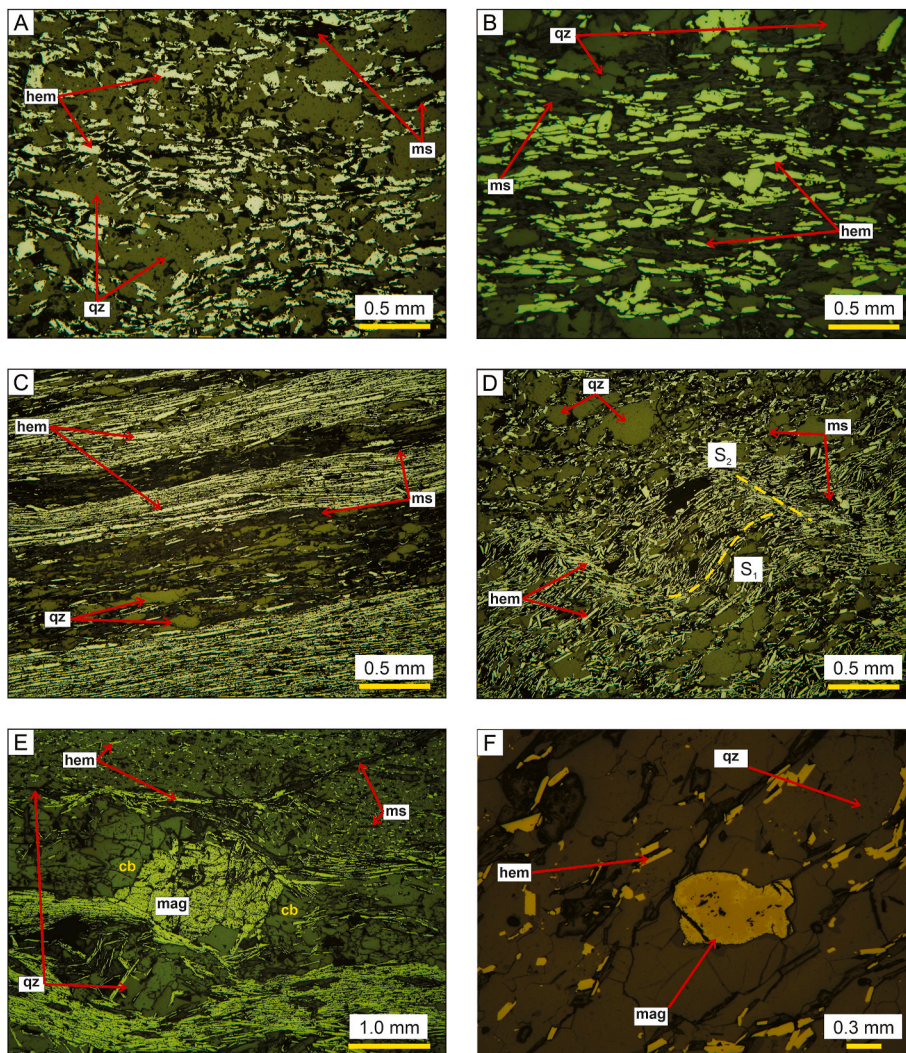
Fig. 9. Photomicrographs of hematite-rich metadiamictites under reflected light (cb, carbonate; hem, hematite; mag, magnetite; ms, muscovite; qz, quartz): A) Fine-grained specular hematite outlining the S_1 foliation that envelops recrystallized quartz and rare granular hematite; B) Band rich in fine-grained specular hematite along S_1 foliation; C) Specularite-rich and hematite-poor bands, parallel to S_1 foliation; D) S_2 crenulation foliation with recrystallized specular hematite, cutting S_1 schistosity; E) Stretched porphyroblast of martitized magnetite with specularite-bearing recrystallization tails; F) Deformed magnetite bounded by recrystallized quartz.

between 7.55 and 45.04 wt%, reaching up to 78.02 wt% in samples from the ductile shear zones (Fig. 7E and F). Magnetite-rich metadiamictite matrix has Fe_2O_3 between 7.91 and 34.46 wt% with the highest contents given by magnetite-specularite-rich samples from ductile shear zones. MnO content is generally low (0.7 wt%) but rarely reaches up to 9 wt% in magnetite-rich DIF from high-strain zone. CaO, K_2O and MgO, up to 8 wt% in total, are related to carbonate, feldspars and mica contents. Low P_2O_5 (<1 wt%) corroborates apatite scarcity in all iron-rich metadiamictites. Even though metadiamictites are poor in apatite, drill cores in Block 8 show abnormal phosphorus concentrations towards the base of the ore section, close to the basal hematite-rich shear zone (Fig. 5) and in Block 7, the highest concentrations of phosphorus occur in the magnetite-rich metadiamictites with high iron grades, found in high strain zones.

5.1.2. Rare earth elements (REE + yttrium) patterns

The REE patterns for the matrices of iron-rich and barren metadiamictites are similar to PAAS – Post-Archean Australian Shale (Fig. 12, Table 1), showing rather flat trends with $Pr_{(SN)}/Yb_{(SN)}$ ratios around 1 (Fig. 12A–C, 13). Although the iron-rich metadiamictites are slightly depleted in light REE ($Pr_{(SN)}/Yb_{(SN)} < 1$), they also display roughly flat patterns ($Pr_{(SN)}/Yb_{(SN)} \sim 0.9–1.0$) similar to PAAS (Fig. 12B and C). Among the hematite-rich metadiamictite samples, those with alumina content lower than 1% are more depleted in light REE, showing somewhat more fractionated REE patterns (average $Pr_{(SN)}/Yb_{(SN)} = 0.35$)

(Fig. 12B), in agreement with their lower mica content (with Pearson's correlation coefficient between Al_2O_3 wt% and $Pr_{(SN)}/Yb_{(SN)}$ r = 0.9). However, a very low-alumina (0.32 wt%) hematite-rich metadiamictite (12 wt% Fe) shows significant depletion in light REE in relation to heavy REE ($Pr_{(SN)}/Yb_{(SN)} = 0.15$) (Fig. 12B; sample B7F50AM4A in Supplementary data A). Samples of magnetite-rich metadiamictite also show flat REE patterns, with the magnetite DIF richest in iron also displaying a slightly depletion in light REE and fractionated pattern ($Pr_{(SN)}/Yb_{(SN)} < 1$), (Fig. 12C). Furthermore, all metadiamictite samples show REE patterns very distinct from modern hydrothermal fluids (Fig. 12). No significant Cerium anomalies for Pr/Pr*~1 were observed in the analyzed samples (Fig. 13).

5.2. U–Pb geochronology and Hf isotopes

5.2.1. Zircon U–Pb data

Most detrital zircon grains from the iron-rich metadiamictite (MRP1) and biotite-muscovite-quartz schist (Geocron-1) show internal oscillatory zoning typical of igneous rocks (Fig. 14).

5.2.1.1. Hematite-rich metadiamictite (sample MRP1).
Seventy-eight zircon grains, ranging from 85 to 345 μm in length, were recovered from sample MRP1 to perform U–Pb analyses (Supplementary data B). Most of them are rounded to sub-rounded, indicating sedimentary transport, but there are also some euhedral prismatic grains. No specific
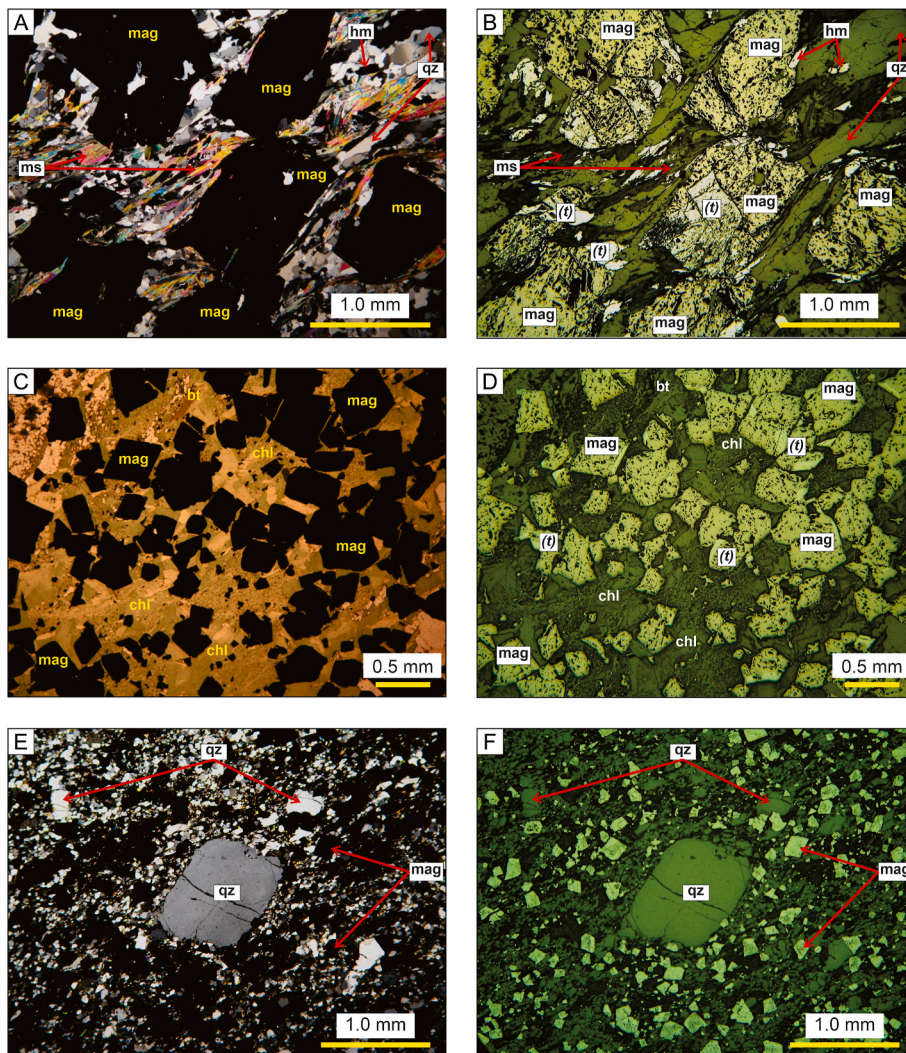
Fig. 10. Photomicrographs of magnetite-rich meta-diamictite under plane-polarized (A) and crossed-polarized (A, E) transmitted light, and corresponding photos under reflected light (B, D, F). Minerals: bt, biotite; chl: chlorite; hem: hematite; mag, magnetite (t, martitized domains); ms: muscovite; qz, quartz. A and B: stretched, coarse-grained, partially martitized magnetite porphyroblasts enveloped by stretched quartz and muscovite outlining S$_1$ schistosity. C and D: euhedral to subhedral magnetite porphyroblasts in chlorite-rich matrix. E and F: euhedral to subhedral, fine-grained magnetite in quartz-rich matrix, enveloping a rounded-shaped quartz grain.

correlation between morphology and internal structure with grain ages was observed (Fig. 14A). The $^{207}Pb/^{206}Pb$ ages range from 930 Ma to 2455 Ma with age peaks at 973 ± 11 Ma (5%), 1256 ± 5 Ma (19%), 1515 ± 6 Ma (14%), 1813 ± 6 Ma (12%), 1978 ± 4 Ma (25%) and 2139 ± 4 Ma (25%) (Fig. 15A). The youngest grain was dated at 930 ± 24 Ma.

5.2.1.2. Biotite-muscovite-quartz schist (sample Geocron-1). Among 112 zircon analyzed grains, 95 provided reliable results with more than 90% concordance for sample Geocron-1 (Supplementary data B). They are mostly rounded and sub-rounded grains up to 200 μm in length, and minor elongated prismatic grains with rounded edges, attesting sedimentary transport. Again, there is no age correlation with grain morphological and textural features (Fig. 14B). The U–Pb ages range from 879 Ma to 3250 Ma with age peaks at 953 ± 15 Ma (11%), 1237 ± 10 Ma (20%), 1521 ± 9 Ma (20%), 1821 ± 8 Ma (24%), 2049 ± 10 Ma (14%), and 2686 ± 11 Ma (11%) (Fig. 15C). The youngest grain was dated at 879 ± 42 Ma.

5.2.2. Lu–Hf data

5.2.2.1. Hematite-rich metadiamictite (sample MRP1). Twenty-eight grains with Mesoproterozoic and Tonian ages were selected for isotope Lu–Hf analyzes from sample MRP1 (Supplementary data B). Overall, εHf$_{(t)}$ values vary from +8.68 to −12.29 (Fig. 15B). Mesoproterozoic grains show Hf T$_{DM}$ model ages from 1600 Ma to 2400 Ma, with mostly

positive (up to +8.68) εHf values for Calymmian grains (with only two exceptions: −0.83 and −2.13), εHf from +6.13 to −7.35 for Ectasian grains, and most negative values up to −8.01 for Stenian zircons with only two positive values up to +3.50. Tonian grains present negative εHf values from −0.25 to −12.29 with Hf T$_{DM}$ model ages ranging from 1790 Ma to 2550 Ma.

5.2.2.2. Biotite-muscovite-quartz schist (sample Geocron-1). Eighty-eight zircon grains were selected for isotope Lu–Hf analyses from sample Geocron-1 (Supplementary data B). Overall, εHf$_{(t)}$ values vary from +6.91 to −23.39 (Fig. 15D). All Archean grains have negative εHf (−1.46 to −8.07) values and Hf T$_{DM}$ model ages ranging from 3140 Ma to 3930 Ma. The oldest Hf T$_{DM}$ model age (3930 Ma) is for a Siderian grain (2434 Ma) with strongly negative εHf value (−19.23). Rhyacian and Orosirian zircon grains mostly show negative εHf values (up to −13.30) and some positive values (up to +4.67), with Hf T$_{DM}$ model ages ranging from 2020 Ma to 3140 Ma. Mesoproterozoic grains show εHf$_{(t)}$ from +6.91 to −17.94, and Hf T$_{DM}$ model ages from 1750 Ma to 3080 Ma. Tonian grains have εHf$_{(t)}$ from −4.63 to −23.39 with only one positive value (+1.64), and Hf T$_{DM}$ model ages from 1640 Ma to 3060 Ma.

6. Discussion

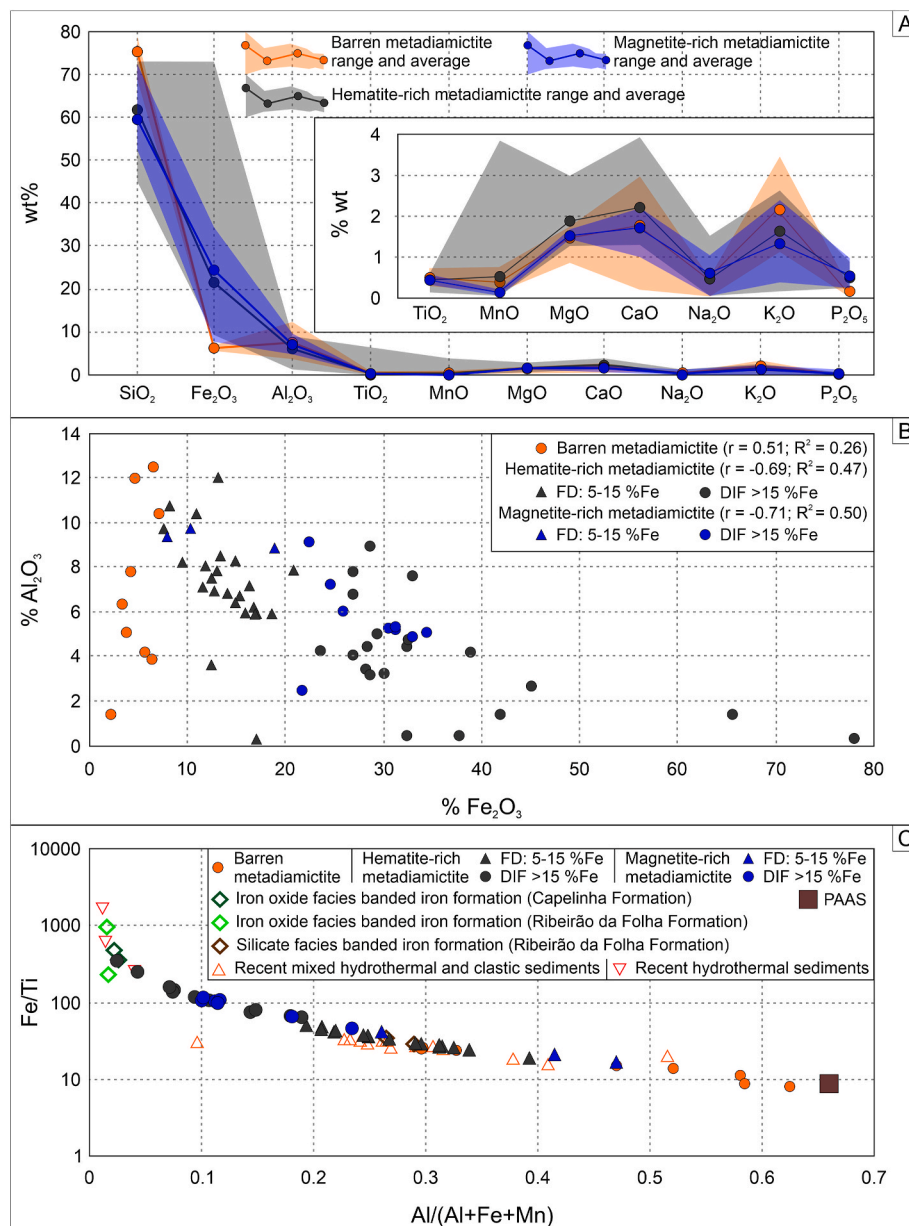Logging data from thousands of meters of borehole drilling cores,

Fig. 11. Lithogeochemistry of matrix samples from iron-rich metadiamictites (DIF and FD) and barren metadiamictites (see Table 2) of the Nova Aurora Iron District: A) Major element diagram; B) Total Fe as Fe_2O_3 versus alumina; and C) Fe/Ti versus Al/(Al + Fe + Mn) (based on Lottermoser and Ashley, 2000). PAAS values from Taylor and McLennan (1985). Data from Neoproterozoic BIFs of the Capelinha and Ribeirão da Folha formations compiled from Pedrosa-Soares (1995) and Queiroga (2006). Recent mixed hydrothermal and clastic sediments and recent hydrothermal sediments are from Dias and Barriga (2006).

together with outcrop information, have revealed iron deposits hosted in metamorphosed clastic rocks with ore bodies consisting of hematite-rich and/or magnetite-rich metadiamictites in the Nova Aurora Iron District; thus, lacking the typical Rapitan banded iron formation features. Preserved sedimentary structures (e.g., fining-up graded bedding, clast size classification, load structures), textures (e.g., rudite fabrics with scattered oversized clasts, matrix grains and clasts with rounded shape) and polymict rudite composition indicate the studied deposits represent mass (debris) flows and turbiditic sedimentation in a marine setting regionally correlated with a glaciation event recorded by the Macaúbas Group (e.g., Moraes and Guimarães, 1931; Isotta et al., 1969; Rocha-Campos and Hasui, 1981; Gravenor et al., 1984; Karfunkel and Hoppe, 1988; Pedrosa-Soares et al., 1992, Pedrosa-Soares et al., 2011a; Uhlein et al., 1998, 1999).

6.1. Depositional environment and implications for Sturtian glaciation-related iron formation

Although the studied iron-rich metadiamictites and other Neoproterozoic iron formations show similar iron oxide assemblage, there are several differences among them, mainly in rock types and related features (Table 1). The studied iron-rich metadiamictites are essentially composed of quartz, hematite and/or magnetite and muscovite (a mineral assemblage clearly correlated with their high contents of iron, silica and alumina) with common accessory minerals like feldspar, carbonate and apatite (Fig. 11A; Tables 1 and 2). Generally, fine-grained hematite is the main ore mineral in glaciation-related Neoproterozoic iron formations, whilst the studied iron-rich metadiamictites display coarser-grained (up to 1 mm in length) hematite owing to metamorphic recrystallization under garnet zone P-T conditions in the greenschist facies (Table 1). In most Neoproterozoic IF, the iron oxides and gangue minerals cluster in distinct and alternated laminae and bands, forming laminated IF and banded iron formation (BIF). Conversely, the studied diamictitic iron formations (DIF) and associated ferruginous metadiamictites show hematite and/or magnetite disseminated in the rock matrix, with specular hematite flakes marking the S_1 and S_2 foliations that envelop or are cut by scattered grains of granular hematite and magnetite porphyroblasts. Concerning
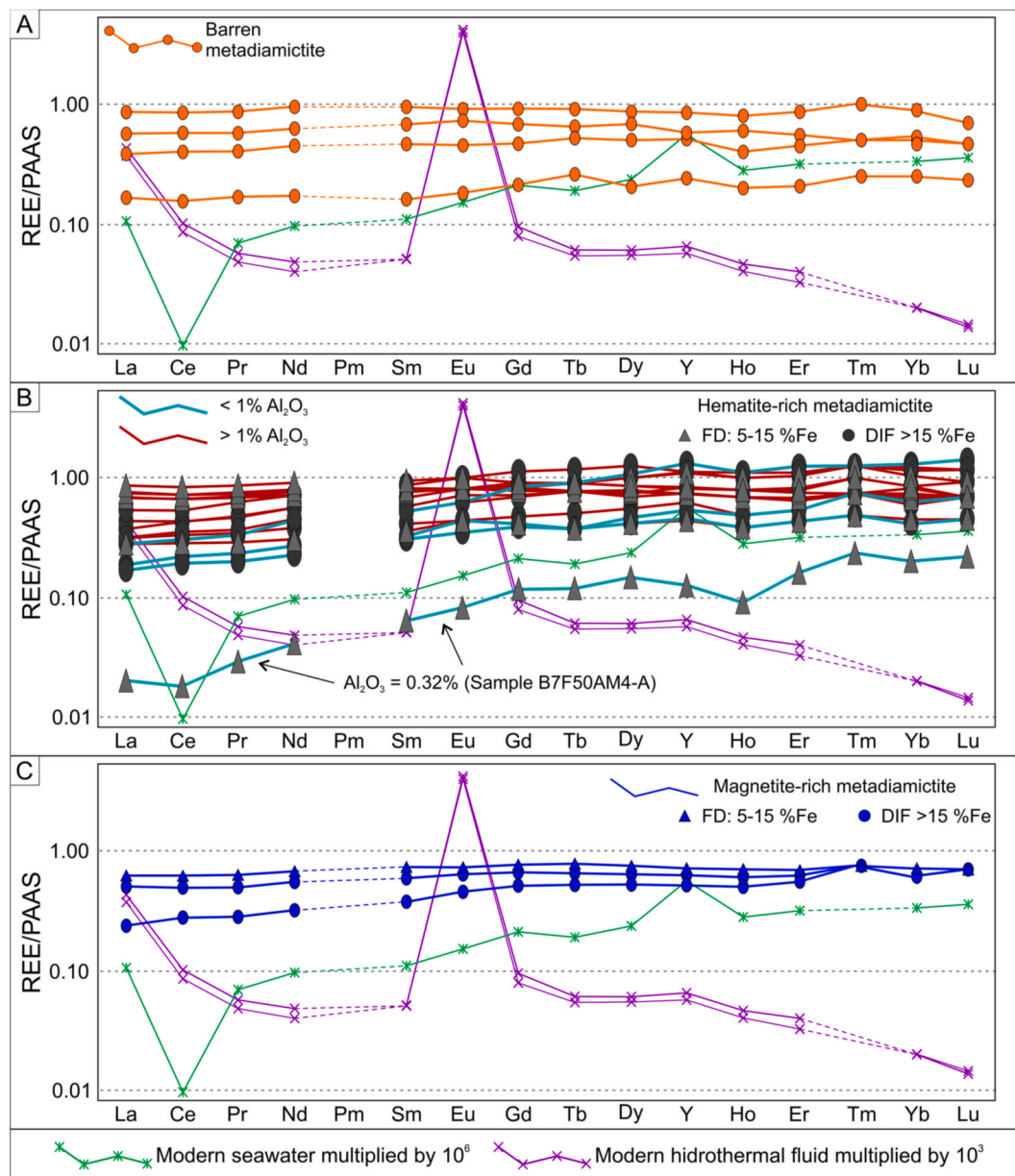
Fig. 12. REE (rare earth elements plus Y) patterns normalized to PAAS (cf. Taylor and McLennan, 1985) for matrix samples of: A) Barren metadiamictite; B) Hematite-rich metadiamictite (indicating the sample with the lowest Al_2O_3 concentration); C) Magnetite-rich metadiamictite. Data for modern seawater (x 10^6) and modern hydrothermal fluid (x 10^3) are from Douville et al. (2002).

rock types, the Nova Aurora Iron District only shows iron-rich rudites, i. e., DIF and associated ferruginous metadiamictites (Table 2), whereas clast-free laminated and banded iron formations prevail in virtually all other deposits of glaciation-related Neoproterozoic iron formations (Table 1). Furthermore, the studied DIF and ferruginous metadiamictites are free of any clasts from iron-rich rocks and minerals, attesting that hematite and magnetite were not directly provided by detrital sediments. In contrast, the massive ferruginous diamictite interleaved with the Chuos and Holowilena iron formations shows ferruginous siltstone intraclasts that have been interpreted as detrital contribution of iron-rich mud supplied by tectonically-induced turbidity currents and mass flows (Lechte and Wallace, 2016). The Nova Aurora iron-rich diamictite deposits represent high-energy (debris flows to turbidites) distal glaciomarine sedimentation, contrasting with the typical Rapitan iron formation formed in low-energy, relatively stable, shallow glaciomarine environments (Table 1).

In both hematite-rich and magnetite-rich metadiamictites Al_2O_3 and

$Fe_2O_{3(t)}$ concentrations display negative correlations with Pearson's correlation coefficient (r) around −0.7 and R^2 ~0.5 (Fig. 11B), while the barren metadiamictite has moderately positive correlation (r = 0.51 and R^2 = 0.26). By using the Fe/Ti vs Al/(Al + Fe + Mn) relation (cf. Lottermoser and Ashley, 2000; Cox et al., 2013; Feng et al., 2017), the barren and iron-rich metadiamictites are compared to recent hydrothermal and mixed (hydrothermal plus clastic) sediments, the Post-Archean Australian Shale – PAAS, and to non-glaciogenic iron formations of the Macaúbas Group (Fig. 11C; Table 1). High Fe/Ti and Fe/Al ratios are typical of hydrothermal fluids because aluminum and titanium are essentially insoluble in seawater and resilient to hydrothermal alteration (Feng et al., 2017, and references therein). Actually, the iron-rich metadiamictites span from the hydrothermal sediments end-member to the PAAS (pelite) zone through the wide domain of mixed (clastic-hydrothermal) sediments (Fig. 11C), suggesting that iron was supplied by both hydrothermal and detrital sources. Conversely, the barren metadiamictite samples cluster around the PAAS, suggesting
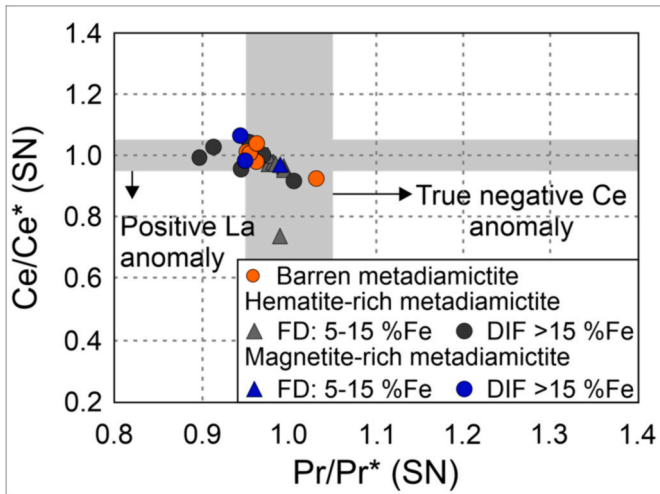
Fig. 13. Pr/Pr*$_{(SN)}$ versus Ce/Ce*$_{(SN)}$ diagram for iron-rich and barren metadiamictites, showing no true negative Ce anomaly (based on Planavsky et al., 2010).

silicates (e.g., biotite and tourmaline). As expected, the non-glaciogenic Macaúbas (Capelinha and Ribeirão da Folha) BIF plot in the hydrothermal sediments zone (Fig. 11C; Table 1).

Recrystallization processes along shear zones at the base of iron deposits point to hydrothermal activity associated with the D$_1$ deformation phase. Conversely, progressive hematite depletion against increase in muscovite, magnetite and sulfide towards the top of iron-rich metadiamictite piles suggest gradual changing from oxidizing to reduction conditions during sedimentation (Fig. 5). In fact, the greatest iron enrichment resulted from specularite recrystallization during the main mylonitic deformation associated with selective mineral leaching process. This deformation also induced tectono-metamorphic enrichment of phosphorous indicated by higher P$_2$O concentrations towards the basal hematite-rich shear zone in Block 8 (Fig. 5).

The REE patterns also record pelite (mud) contribution (given by alumina content from mica and other Al-rich silicates) in relation to silica (quartz) and iron contents in metadiamictite matrices. The higher the alumina content, the greater the REE content and the flatter the REE pattern (in relation to PAAS). On the other hand, metadiamictites richer in both silica (quartz) and iron oxide (hematite and/or magnetite), and poorer in alumina (i.e., in mica) tend to display lower REE contents and lower REE mass fractions compared to the rocks richer in alumina and PAAS normalized patterns depleted in LREE (Fig. 12). They also show no
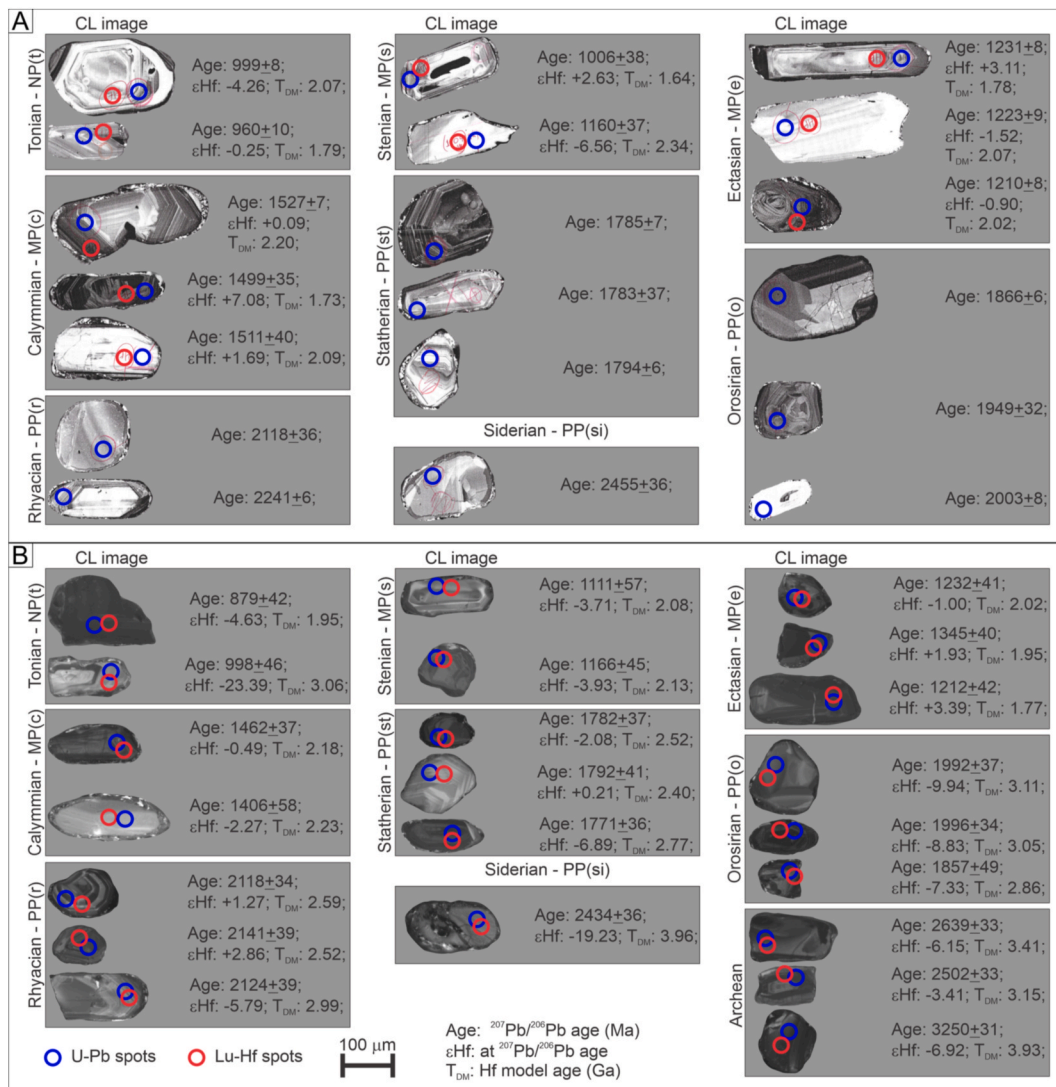
their low iron content is given by clastic components like iron-rich

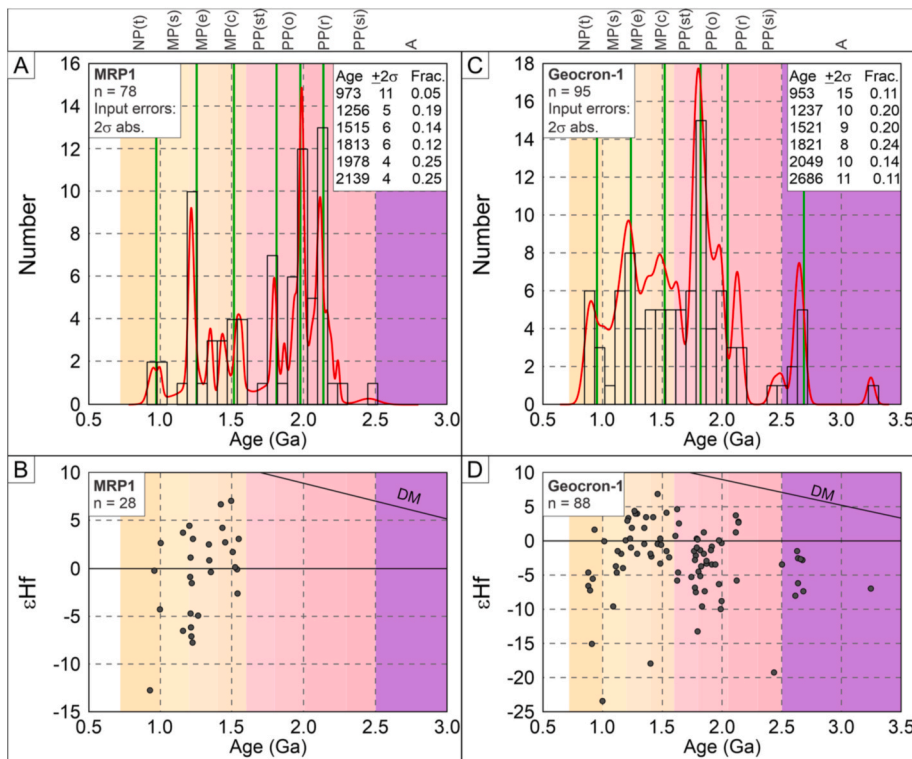**Fig. 14.** Representative CL images of detrital zircons for samples: A) MRP1; B) Geocron-1.

Fig. 15. U–Pb and Lu–Hf diagrams. Background colors for time divisions according to the International Stratigraphic Chart (2019): NP(t), Tonian; MP (s), Stenian; MP(e), Ectasian; MP(c), Calymmian; PP (st), Statherian; PP(o), Orosirian; PP(r), Rhyacian; PP (si), Siderian; A, Archean. DM, depleted mantle. Sample MRP1: A) Frequency histogram and probability curve; B) εHf versus age (only for Mesoproterozoic and Neoproterozoic grains). Sample Geocron-1: C) Frequency histogram and probability curve; D) εHf versus age.

anomalies of Ce or Y (Fig. 12). Despite their close relation to late hydrothermal activity in high-strain zones magnetite-rich metadiamictites show similar PAAS normalized patterns as the hematite-rich metadiamictites. Furthermore, the REE patterns for studied metadiamictites also lack significant Eu anomaly (Fig. 12B and C), similarly to REE patterns for modern seawater and most Neoproterozoic iron formations (Fig. 16). Indeed, all REE patterns together with major elements composition from the studied metadiamictites contrast with geochemical signatures for modern hydrothermal fluids and non-glaciogenic iron formations (Figs. 11–13 and 16). Besides, the absence of iron-rich clasts in the studied metadiamictites suggests that iron was not provided by detrital sediments to the glaciomarine basin.

Despite hematite recrystallization and enrichment in the basal shear zones, a post-depositional hydrothermal mineralization is unlikely because the: i) lacking of iron oxides in the regional metadiamictites and their quartzite and metapelite intercalations, as well as in the quartzite and metapelite lenses hosted by the iron-rich metadiamictites (Fig. 7D); ii) absence of reaction, replacement, coating and/or fracture and cleavage fillings by hematite and/or magnetite in the matrices and clasts of the barren and iron-rich metadiamictites; and iii) absence of veins swarms, and fracture coatings and fillings by iron oxide or any other feature suggesting hydrothermal conduits cutting across the barren and iron-rich rocks. Actually, iron-rich fluids coming through the basal shear zones would have also percolated the iron-barren rocks, leaving evidence of iron oxide deposition. Furthermore, post-depositional hydrothermal fluids that would have passed through the iron-rich metadiamictite matrix should also have percolated and deposited iron oxide into the quartzite lenses or, at least, have left some evidence of an iron-rich fluid cutting across them. Additionally, no evidence of mineral replacement or corrosion or coating by iron oxide was observed in matrix primary grains and clasts of any studied metadiamictite, not even in the more reactive rock clasts (such as carbonates). Indeed, none of all those possible evidences for a hydrothermal process were ever observed in any studied sample, outcrop or drill core section, and no mention on at least one of them are found in the available literature. As a corollary, the iron-barren rocks would represent the basin sites and time intervals

free of iron precipitation during the sedimentation of the iron-rich diamictites. Therefore, the presented evidence suggest that anomalous iron amounts were available in seawater during the deposition of diamictitic mass (debris) flows in the glaciomarine basin sector now exposed in the Nova Aurora Iron District.

Virtually all metadiamictite samples lack true negative Ce anomaly for $Pr/Pr^* \sim 1$ (Fig. 13), indicating seawater under oxygen-poor to anoxic conditions and, thus, enriched in soluble ferrous (Fe^{2+}) iron (Feng et al., 2017, and references therein). A later change in seawater to a somewhat oxygenated condition could enable ferrous iron oxidation and deposition as ferric (Fe^{3+}) iron together with the diamictitic protoliths. In that oxygen-poor environment cerium would be present in its trivalent state (Ce^{3+}) and the redox potential change may not have been strong enough to promote the oxidation from Ce^{3+} to Ce^{4+}, explaining the lack of negative Ce anomaly (Lechte et al., 2018b and references therein). An expected scenario for those processes envisages ice cap thawing during deglaciation, supplying oxygenated waters to the marine basin. Continental-scale deglaciation causes sea level rise and marine transgression, resulting in massive input of oxygen-rich water in glaciomarine basins. This promotes rapid oxidation of the available ferrous iron and deposition of hematite-rich sediments in the lower sedimentary successions. Indeed, the fining-up depositional record from quartz-rich (sandy)-matrix metadiamictite with graded sandstone lenses, gradually passing to mica-rich(pelitic)-matrix metadiamictite with metapelite intercalations, points to marine transgression drowning the glaciomarine basin. As iron and oxygen were quickly consumed in the early transgression stage, they became relatively scarce, resulting in the decrease in the iron content and favoring magnetite deposition followed by sulfide toward the top of the diamictitic pile (Figs. 2, 5 and 6). Rising in mud-rich fraction and decreasing in oxidizing conditions have been related to marine transgression in deposits of glaciation-related iron formations elsewhere, such as the classic Rapitan and Halowilena deposits (Klein and Beukes, 1993; Cox et al., 2016).

The PAAS-normalized REE distributions (Fig. 16B) for Neoproterozoic iron formations show patterns similar to those observed in the Nova Aurora DIF and ferruginous metadiamictites, displaying slight
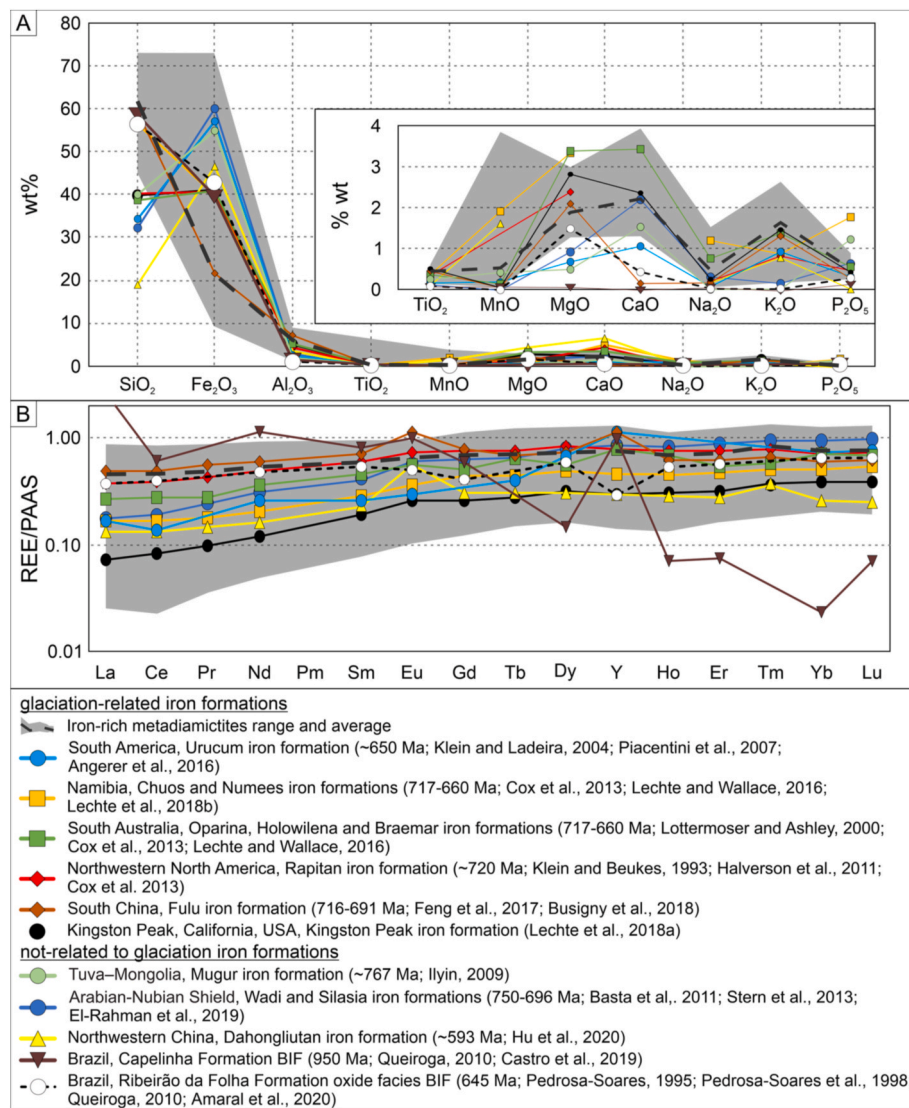
Fig. 16. Comparison of lithogeochemical signatures for studied iron-rich metadiamictites and Neoproterozoic iron formations from several places around the world.

depletion in LREE and variable Eu anomalies (1.00–2.56; Fig. 16B). Absent to small Eu anomalies characterize most Neoproterozoic glaciogenic iron formations, implying in none or little iron contribution from hydrothermal fluids (especially those of high temperature). Conversely, prominent Eu anomalies (up to 2.37) shown by non-glaciogenic iron formations are related to hydrothermal-exhalative processes similar to those associated with Algoma-type BIF (Fig. 16). Most Neoproterozoic iron formations show slightly negative Ce anomalies (Fig. 16), indicating mildly oxidizing environment (Feng et al., 2017).

6.2. Maximum depositional age and sediment provenance

U–Pb ages for detrital zircon grains from samples of the studied iron deposits show wide distributions akin to age spectra for continental rift and passive margin basins (cf. Cawood et al., 2012), like the age spectra for the Macaúbas basin stages (Fig. 17A and B). The Macaúbas basin system includes two continental rift stages and a passive margin stage evolved to oceanic setting (Pedrosa-Soares and Alkmim, 2011; Pedro-sa-Soares et al., 2011a, 2020; Kuchenbecker et al., 2015; Peixoto et al., 2015; Amaral et al., 2020). The Early Tonian rifting event (rift 1) started around 940 Ma and aborted at ca. 870 Ma, forming an aulacogen filled with the diamictite-free (pre-glacial) units of the Macaúbas and Santo

Onofre groups (Babinski et al., 2012; Costa and Danderfer, 2017; Castro et al., 2019; Souza et al., 2019), including the Rio Peixe Bravo Formation located in the study area (Fig. 1C). In the West Congo Belt, the counterpart of the Araçuaí Orogen located in central-southwest Africa, the Early Tonian Zadinian-Mayumbian volcano-sedimentary succession with bimodal anorogenic magmatism dated between 930 and 890 Ma (Tack et al., 2001; Frimmel et al., 2006; Pedrosa-Soares et al., 2016; Thiéblemont et al., 2018) corresponds to the Macaúbas rift 1 and associated anorogenic magmatism (Fig. 18A) (Pedrosa–Soares et al., 2008; Pedrosa-Soares et al., 2011a; Castro et al., 2019).

Long after, at the Tonian–Cryogenian boundary, another continental rifting event started and formed a basin filled by the glaciogenic units of the Macaúbas Group (Figs. 17 and 18), including the glaciomarine Nova Aurora Formation and its iron-rich diamictite deposits with maximum sedimentation ages around 880 Ma (Pedrosa-Soares and Alkmim, 2011; Pedrosa-Soares et al., 2011a; Kuchenbecker et al., 2015). However, the sedimentation age of the Macaúbas glaciomarine diamictites was more precisely constrained between 720 and 670 Ma (Castro et al., 2020). This agrees with correlations of the Macaúbas diamictites to the Lower Diamictite Formation, a glaciogenic unit of the West Congo Belt enclosing volcanic rocks aged at around 700 Ma (Pedrosa–Soares et al., 2008, Pedrosa-Soares et al., 2011a; Straathof, 2011; Thiéblemont et al., 2009a, 2009b, 2018). Accordingly, Early Cryogenian is the most
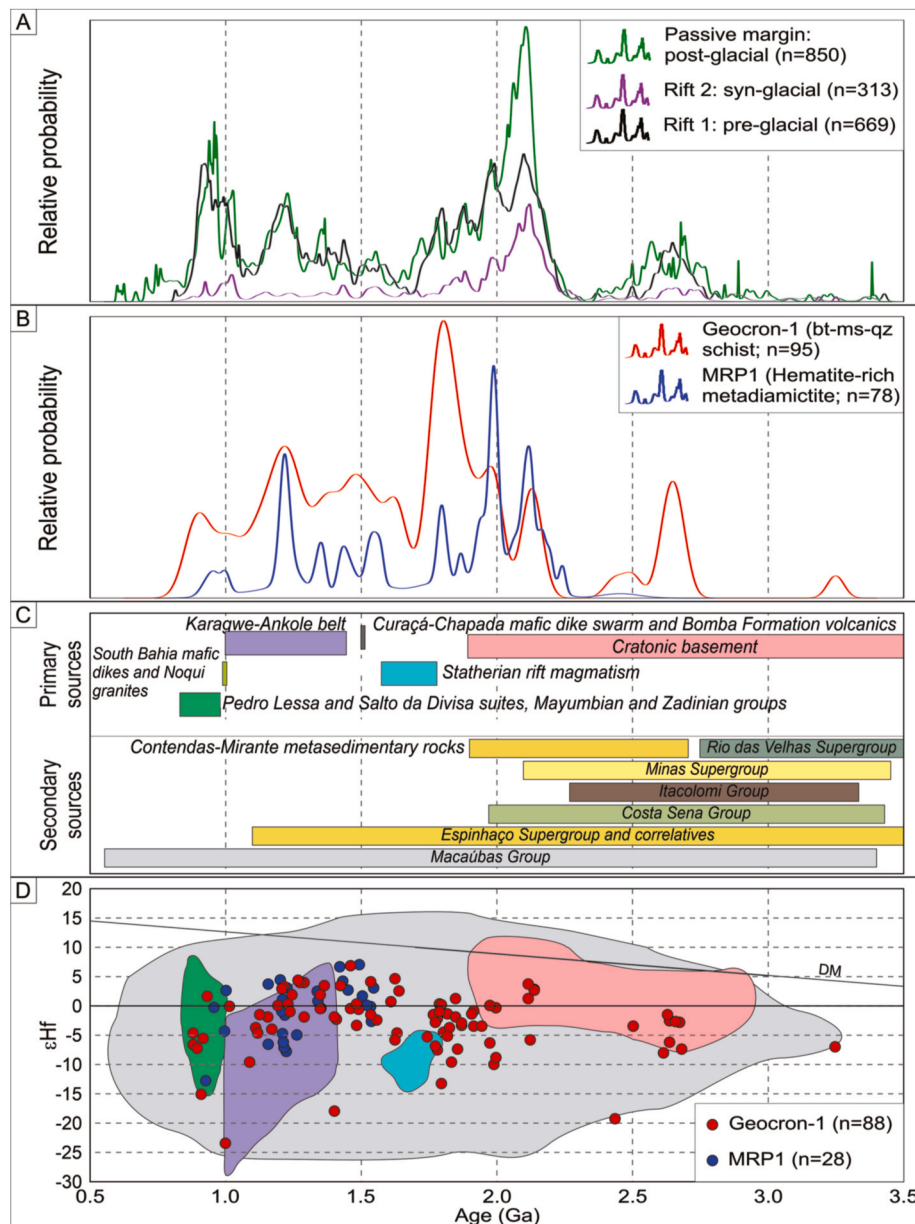
Fig. 17. – A) U–Pb age spectra from detrital zircons for distinct stages of the Macaúbas basin system (cf. Pedrosa-Soares et al., 2020); B) Age spectra for detrital zircon grains from samples of the Nova Aurora Iron District (samples Geocron-1 and MRP1); C) Time span bars for primary and secondary zircon sources for the analyzed samples of the Nova Aurora Iron District (adapted from Kuchenbecker et al., 2015, and updated after Pedrosa-Soares et al., 2020, and Lombello, 2020); D) εHf versus age scatter diagram for the analyzed samples, compared to εHf fields for possible zircon sources (light grey field includes all secondary sources; colors for primary source field according to Fig. 17C). Compiled data from data from Albert et al. (2016), Amaral et al. (2020), Castro et al. (2019, 2020), Gomes et al. (2020), Magalhães et al. (2018), Moreira (2017), Pacheco et al. (2021), Schannor et al. (2019, 2020), Souza (2016) and Tack et al. (2010).

probable depositional age for the studied iron-rich diamictites, thus relating them to the global Sturtian glaciation event (Pedrosa-Soares et al., 2011a; Babinski et al., 2012; Castro et al., 2020).

For sediment provenance assessments, the U–Pb and Lu–Hf data from detrital zircon samples of the studied iron deposits are compared to data from rock units exposed in the Araçuaí – West Congo orogenic system (AWCO), and São Francisco and Congo cratons (Figs. 15 and 17). Reliable primary sources for Archean to Orosirian zircon grains are the migmatitic-gneissic complexes, related intrusions and supracrustal rock assemblages found in AWCO basement and related cratons (Teixeira et al., 2015; Silva et al., 2016; Bersan et al., 2018, 2020; Degler et al., 2018). The Statherian–Stenian Espinhaço basin system might have acted as an important secondary sediment source (Fig. 17C), supplying detrital zircon grains as old as 3.4 Ga (Chemale Jr. et al., 2012). Most detrital zircon grains of Statherian and Mesoproterozoic ages might be supplied by the anorogenic magmatic rocks related to the Espinhaço rift basin (specially the zircon grains with negative εHf from −5 to −15; Fig. 17) and by mafic dike swarms located in the region covered by the São Francisco Craton and Araçuaí Orogen (Danderfer et al., 2009; Chemale

et al., 2012; Guadagnin and Chemale, 2015; Magalhães et al., 2018; Caxito et al., 2020). Mesoproterozoic zircon grains with positive εHf values could have been supplied by mafic dyke swarms found in the São Francisco Craton and Araçuaí Orogen (Silveira et al., 2013; Fonte-Boa et al., 2017; Caxito et al., 2020) and juvenile igneous rocks of the Karagwe-Ankole belt (cf. Degler et al., 2017, and references therein).

The most reliable sources for the Early Tonian zircon grains with negative εHf values is the large amount of anorogenic bimodal volcanic rocks and related intrusions associated with the aborted Macaúbas rift 1, and its counterpart located in the West Congo belt (Pedrosa-Soares et al., 2000, 2020; Tack et al., 2001; Frimmel et al., 2006; Silva et al., 2008; Chaves et al., 2019; Castro et al., 2019; Souza et al., 2019; Moreira et al., 2020). Actually, the Early Tonian anorogenic igneous rocks would have been exposed and eroded after shoulders and horsts uplift during rift 2 development in the Early Cryogenian, thus supplying sediments to Macaúbas glaciogenic units, such as the iron-rich diamictitic deposits.

Although they have not been dated yet owing to the lack of zircon grains, thin lenses of chlorite schist with high Fe, Mg, Cr, Ni and Cu contents suggest volcanic ash contribution during the basin evolution
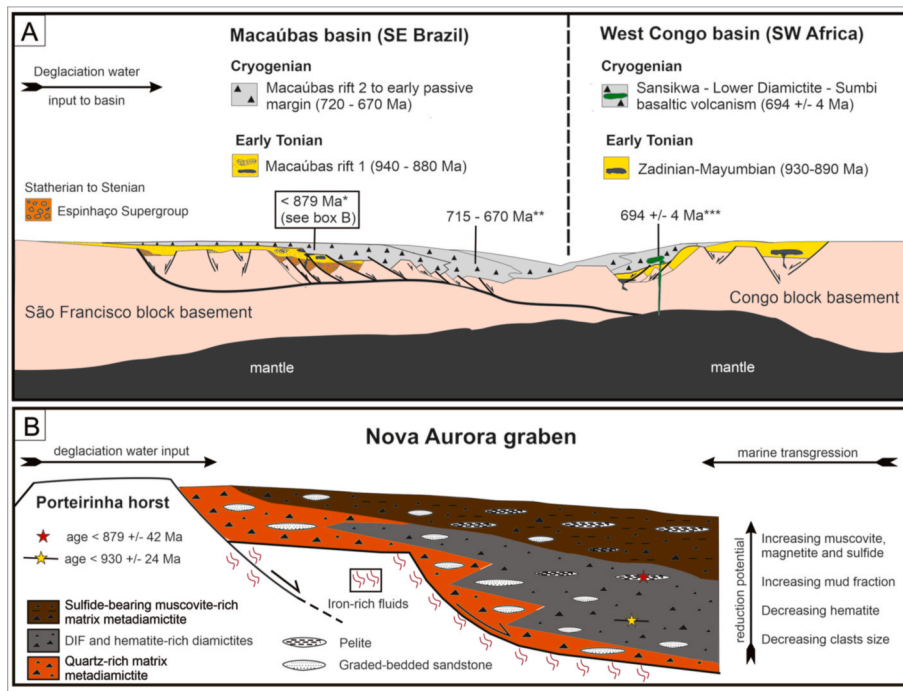
Fig. 18. – A) Correlation sketch section showing counterparts of the Macaúbas and West Congo basins (modified and simplified after Pedrosa–Soares et al., 2008, and Castro et al., 2020; updated with data from Thiéblemont et al., 2018, and Pedrosa-Soares et al., 2016, 2020). U–Pb ages quoted along section are from this paper *, Castro et al. (2020)**, and Straathof (2011)***. B) Horst-graben model for the relatively restrict sector of the Macaúbas glaciomarine basin where the Nova Aurora Iron District developed (see text for detailed explanations).

(Vilela, 2010).

6.3. Model for the Nova Aurora Iron District

Based on the lithological association, regional and local sedimentary environments, Fe-rich mineral assemblages and textures, petrographic features, lithogeochemistry and isotopic data from the metadiamictitic iron-rich deposits, compared to compiled data, we present the following model for the Nova Aurora Iron District and DIF deposits (Fig. 18).

The presented geological scenario and analytical dataset allow us to envisage a relatively restrict sector, filled by iron-rich deposits, within the large Macaúbas glaciomarine basin. That restrict basin sector was a graben formed in the Macaúbas rift 2 stage, the Nova Aurora graben, bounded by the Porteirinha horst at the proximal (west) side (Fig. 18B). The Nova Aurora graben was filled by sediments provided by far continental sources, as well as by sediments eroded from the rift shoulders and internal horsts. Deposited in subsiding grabens, the regional (basal) sandy-matrix diamictites represent the early mass flows triggered by active faults associated with the uplift of rift shoulders and horsts. The Porteirinha horst was uplifted under glacial conditions and imposed restrictions to water circulation with concomitant ferrous iron accumulation under anoxic conditions in the Nova Aurora graben. Iron could have been extracted from the basement (e.g., mafic-ultramafic and TTG complexes) and supracrustal rocks (e.g., mafic volcanic rocks of the Macaúbas rift 1 and Espinhaço Supergroup) by fluid circulation along active fault zones and then, discharged in seawater under anoxic conditions. Glacier thawing in the São Francisco continental region (to the west), and on uplifted rift shoulders and internal horsts supplied large amounts of oxygen-rich waters to the basin, promoting rapid and voluminous precipitation of ferrous iron as iron hydroxides, together with the deposition of initially clay-poor debris flows with high-density turbidite lenses that became gradually enriched in mud fraction. Progressive deglaciation in a basin evolving from rift to passive margin triggered widespread sea level rising and marine transgression toward the Porteirinha horst, drowning the Nova Aurora graben with mud-rich mass flows and turbidites, under decreasing oxidizing conditions (Fig. 18B). Therefore, the deeper the layer the richer in iron is the diamictite in the Nova Aurora deposits.

During basin inversion by compressive tectonics, the syn-kinematic metamorphism recrystallized the iron hydroxides and oxides along ductile foliations and mylonitic shear zones, forming hematite-rich metadiamictites. The diamictites formerly richest in iron oxide (mostly hematite) are also those that better accommodated the ductile deformation at the base of the iron deposits, forming Fe-enriched DIF in high strain zones after gangue minerals removal.

Progressive deformation along high-strain zones triggered significant Fe remobilization at a late metamorphic-hydrothermal stage, forming magnetite-rich DIF. Strong positive correlation between Fe_2O_3 and P_2O_5, with Pearson's correlation coefficient r = 0.8 (Fig. 6), suggests phosphorus concentration during the metamorphic-hydrothermal process that formed magnetite-rich metadiamictite in ductile shear zones.

7. Conclusions

- The Nova Aurora Iron District comprises large deposits of iron-rich diamictites, including typical diamictitic iron formation (DIF: Fe > 15 wt%), metamorphosed in the garnet zone of greenschist facies. The prevailing hematite-rich metadiamictites (7–60 vol% hematite in matrix) with total Fe between 5 and 45 wt% show local iron enrichment up to 78 wt% in ductile shear zones. The magnetite-rich metadiamictite is restricted to high-strain ductile shear zones with late metamorphic-hydrothermal recrystallization. Total reserves reach over 20 billion metric tons of low-grade iron ore (17–35 wt% Fe).
- The protoliths of the iron-rich and barren metadiamictites with quartzite and metapelite lenses are mass (debris) flow deposits and high-to-low energy turbidites. The barren metadiamictite rich in sandy matrix and the metadiamictites richest in hematite record high-energy environment under relatively stronger oxidizing conditions. The fining-up graded sedimentation with upwards enrichment in mud fraction, and the base-to-top depositional succession of hematite, magnetite and sulfide in the iron-rich diamictite pile suggest a transgression event with gradually less oxidizing conditions toward the top of the iron deposits.
- Evaluation of mineral assemblages coupled with lithogeochemical data from the metadiamictites suggests ferrous iron accumulation in

seawater under anoxic to suboxic conditions in an ice-caped basin. The influx of oxygen-rich water from glaciers meltdown to the basin triggered iron oxide precipitation from seawater, together with the deposition of initially clay-poor debris flows which gradually became enriched in mud fraction. The highest concentration of hematite in the deepest DIF layers suggests voluminous influx of oxygen-rich water provided by rapid ice-cap melting, causing fast precipitation of large iron (oxi)hydroxide amounts in the early deposition stage.

- The magnetite-rich metadiamictite represents secondary iron mineralization formed by late hydrothermal-metamorphic processes in high-strain zones.
- The U–Pb age spectrum and respective Lu–Hf data for detrital zircon grains confirm previous correlations of the Nova Aurora iron-rich metadiamictites with the extensive glaciomarine succession, deposited in the Cryogenian Macaúbas rift (Fig. 18A), which has been correlated to the Sturtian global glaciation (e.g., Babinski et al., 2012; Kuchenbecker et al., 2015; Castro et al., 2020).

Declaration of competing interest

The authors declare that they have no known competing financial interests or personal relationships that could have appeared to influence the work reported in this paper.

Acknowledgments

Appendix A. Supplementary data

Supplementary data to this article can be found online at https://doi.org/10.1016/j.jsames.2021.103614.

Author statement

Francisco Teixeira Vilela: Conceptualization; Investigation; Writing – original draft, Writing – review & editing. **Antonio Pedrosa-Soares:** Conceptualization; Investigation; Resources; Writing – review & editing; Project administration. **Marly Babinski:** Formal analysis; Resources; Funding acquisition; Writing – review & editing. **Cristiano Lana:** Formal analysis; Resources; Funding acquisition; Writing – review & editing. **Ricardo Trindade:** Resources; Funding acquisition; Writing – review & editing. **Eduardo Santos:** Conceptualization; Investigation.

References

Albert, C., Farina, F., Lana, C., Stevens, G., Storey, C., Gerdes, A., Dopico, C.M., 2016. Archean crustal evolution in the Southern São Francisco craton, Brazil: constraints from U-Pb, Lu-Hf and O isotope analyses. Lithos 266–267, 64–86.

Alkmim, F.F., Marshak, S., Pedrosa-Soares, A.C., Peres, G.G., Cruz, S., Whittington, A., 2006. Kinematic evolution of the Araçuaí-west Congo orogen in Brazil and Africa: Nutcracker tectonics during the Neoproterozoic assembly of Gondwana. Precambrian Res. 149, 43–64.

Amaral, L., Caxito, F.A., Pedrosa-Soares, A.C., Queiroga, G., Babinski, M., Trindade, R., Lana, C., Chemale, F., 2020. The Ribeirão da Folha ophiolite-bearing accretionary wedge (Araçuaí orogen, SE Brazil): new data for Cryogenian plagiogranite and metasedimentary rocks. Precambrian Res. 336, 105522.

Angerer, T., Hagemann, S.G., Walde, D.H.G., Halverson, G.P., Boyce, A.J., 2016. Multiple metal sources in the glaciomarine facies of the Neoproterozoic Jacadigo iron formation in the "Santa Cruz deposit". Corumbá, Brazil. Precambrian Research 275, 369–393.

Babinski, M., Pedrosa-Soares, A.C., Trindade, R.I.F., Martins, M., Noce, C.M., Liu, D., 2012. Neoproterozoic glacial deposits from the Araçuaí orogen, Brazil: age, provenance and correlations with the São Francisco craton and West Congo belt. Gondwana Res. 21, 451–465.

Baldwin, G.J., Turner, E.C., Kamber, B.S., 2012. A new depositional model for glacio-genic Neoproterozoic iron formation: insights from the chemostratigraphy and basin configuration of the Rapitan iron formation. Can. J. Earth Sci. 49, 455–476.

Barrote, V.R., Rosière, C.A., Rolim, V.K., Santos, J.O.S., McNaughton, N.J., 2017. As formações ferríferas bandadas proterozoicas de Guanhães, borda sudeste do Cráton São Francisco, Brasil: evidências de contaminação detrítica. Geol. Usp. Série Científica 17 (2), 303–324.

Basta, F.F., Maurice, A.E., Fontboté, L., Favarger, P., 2011. Petrology and geochemistry of the banded iron formation (BIF) of Wadi Karim and um Anab, eastern Desert, Egypt: implications for the origin of Neoproterozoic BIF. Precambrian Res. 187, 277–292.

Bau, M., Dulski, P., 1996. Distribution of yttrium and rare-earth elements in the Penge and Kuruman iron formations, Transvaal Supergroup, South Africa. Precambrian Res. 79, 37–55.

Bekker, A., Krapež, B., Slack, J.F., Planavsky, N., Hofmann, A., Konhauser, K.O., Rouxel, O.J., 2012. Iron Formation: the sedimentary product of a complex interplay among mantle, tectonic, oceanic, and biospheric processes – a reply. Econ. Geol. 107, 379–380.

Bekker, A., Planavsky, N.J., Krapež, B., Rasmussen, B., Hofmann, A., Slack, J.F., Rouxel, O.J., Konhauser, K.O., 2014. Iron formations: their origins and implications for ancient seawater chemistry. In: Holland, H.D., Turekian, K.K. (Eds.), Treatise of Geochemistry, second ed., vol. 9. Elsevier, pp. 561–628.

Bekker, A., Slack, J.F., Planavsky, N., Krapež, B., Hofmann, A., Konhauser, K.O., Rouxel, O.J., 2010. Iron formation: the sedimentary product of a complex interplay among mantle, tectonic, oceanic, and biospheric processes. Econ. Geol. 105, 467–508.

Bersan, S.M., Danderfer Filho, A., Abreu, F.R., Lana, C., 2018. Petrography, geochemistry and geochronology of the potassic granitoids of the Rio Itacambiruçu supersuite: implications for the meso- to Neoarchean evolution of the Itacambira-monte Azul block. Braz. J. Geol. 48, 1–24.

Bersan, S.M., Costa, A.F.O., Danderfer, A., Abreu, F.R., Lana, C., Queiroga, G., Storey, C., Moreira, H., 2020. Paleoproterozoic juvenile magmatism within the northeastern sector of the São Francisco paleocontinent: insights from the shoshonitic high Ba–Sr Montezuma granitoids. Geoscience Frontiers 11, 1821–1840.

Blichert-Toft, J., Albarede, F., 1997. The Lu-Hf isotope geochemistry of chondrites and the evolution of the mantle crust system. Earth Planet Sci. Lett. 148, 243–258.

Breitkopf, J.H., 1988. Iron Formations related to mafic volcanism and ensialic rifting in the southern margin zone of the Damara Orogen, Namibia. Precambrian Res. 38, 111–130.

Busigny, V., Planavsky, N.J., Goldbaum, E., Lechte, M.A., Feng, L., Lyons, T.W., 2018. Origin of the Neoproterozoic Fulu iron formation, South China: insights from iron isotopes and rare earth element patterns. Geochem. Cosmochim. Acta 242, 123–142.

Canfield, D.E., Zhang, S., Wang, H., Wang, X., Zhao, W., Su, J., Bjerrum, C.J., Haxen, E.R., Hammarlund, E.U., 2018. A Mesoproterozoic iron formation. Proc. Natl. Acad. Sci. Unit. States Am. 115 (17), E3895–E3904.

Castro, M.P., Queiroga, G., Martins, M., Alkmim, F., Pedrosa-Soares, A., Dussin, I., Souza, M.E., 2019. An early tonian rifting event affecting the São Francisco-Congo paleocontinent recorded by the lower Macaúbas group, Araçuaí orogen, SE Brazil. Precambrian Res. 331, 105351.

Castro, M.P., Queiroga, G., Martins, M., Pedrosa-Soares, A., Dias, L., Lana, C., Babinski, M., Alkmim, A.R., Silva, M.A., 2020. Provenance shift through time in superposed basins: from Early Cryogenian glaciomarine to Late Ediacaran orogenic sedimentations (Araçuaí Orogen, SE Brazil). Gondwana Res. 87, 41–66.

Cawood, P.A., Hawkesworth, C.J., Dhuime, B., 2012. Detrital zircon record and tectonic setting. Geology 40 (10), 875–878.

Caxito, F.A., Hagemann, S., Dias, T.G., Barrote, V., Dantas, E.L., Chaves, A.O., Campello, M.S., Campos, F.C., 2020. A magmatic barcode for the São Francisco Craton: contextual in-situ SHRIMP U-Pb baddeleyite and zircon dating of the Lavras, Pará de Minas and Formiga dyke swarms and implications for Columbia and Rodinia reconstructions. Lithos 374–375, 105708.

Chaves, A.O., Ernst, R.E., Söderlund, U., Wang, X., Naeraa, T., 2019. The 920-900 Ma Bahia-Gangila lip on the São Francisco and Congo cratons and link with Dashigou-Chulan lip of north China craton: new insights from U-Pb geochronology and geochemistry. Precambrian Res. 329, 124–137.

Chaves, M.L.C., Silva, M.C.R., Scholz, R., Babinski, M., 2013. Grenvillian age magmatism in the southern Espinhaço range (minas Gerais): evidence from U-Pb zircon ages. Braz. J. Geol. 43 (3), 477-48.

Chemale, F., Dussin, I.A., Alkmim, F.F., Martins, M.S., Queiroga, G., Armstrong, R., Santos, M.N., 2012. Unravelling a Proterozoic basin history through detrital zircon geochronology: the case of the Espinhaço Supergroup, Minas Gerais, Brazil. Gondwana Res. 22, 200–206.

CODEMIG-SEDE-CPRM, 2006. Levantamento aerogeofísico de Minas Gerais, Programa 2005/2006. Área 8: Minas Novas – Riacho dos Machados – Espinosa, vol. 1. Relatório final do levantamento e processamento de dados magnetométricos e gamaespectrométricos, Texto técnico, Belo Horizonte, p. 201.

Costa, A.F., Danderfer, A., 2017. Tectonics and sedimentation of the central sector of the Santo Onofre rift, north Minas Gerais, Brazil. Braz. J. Geol. 47 (3), 491–519.

Costa, A.F.O., Danderfer, A., Bersan, S.M., 2018. Record of a statherian rift-sag basin in the central Espinhaço range: facies characterization and geochronology. J. S. Am. Earth Sci. 82, 311–328.

Cox, G.M., Halverson, G.P., Minarik, W.G., Le Heron, D.P., Macdonald, F.A., Bellefroid, E.J., Strauss, J.V., 2013. Neoproterozoic iron formation: an evaluation of its temporal, environmental and tectonic significance. Chem. Geol. 362, 232–249.

Cox, G.M., Halverson, G.P., Poirier, A., Le Heron, D.P., Strauss, J.V., Stevenson, R., 2016. A model for Cryogenian iron formation. Earth Planet Sci. Lett. 433, 280–292.

Danderfer, A., De Waele, B., Pedreira, A.J., Nalini, H.A., 2009. New geochronological constraints on the geological evolution of Espinhaço basin within the São Francisco Craton - Brazil. Precambrian Res. 170, 116–128.

Degler, R., Pedrosa-Soares, A., Dussin, I., Queiroga, G., Schulz, B., 2017. Contrasting provenance and timing of metamorphism from paragneisses of the Araçuaí-Ribeira orogenic system, Brazil: hints for Western Gondwana assembly. Gondwana Res. 51, 30–50.

Degler, R., Pedrosa-Soares, A., Novo, T., Tedeschi, M., Silva, L.Z., Dussin, I., Lana, C., 2018. Rhyacian-Orosirian isotopic records from the basement of the Araçuaí- Ribeira orogenic system (SE Brazil): links in the Congo-São Francisco palaeocontinent. Precambrian Res. 317, 179–195.

Dias, A.S., Barriga, F.J.A.S., 2006. Mineralogy and geochemistry of hydrothermal sediments from the serpentinite-hosted Saldanha hydrothermal field (36°34'N; 33°26'W) at MAR. Marine Geology 225, 157–175.

Douville, E., Charlou, J.L., Oelkers, E.H., Bienvenu, P., Jove Colon, C.F., Donval, J.P., Fouquet, Y., Prieur, D., Appriou, P., 2002. The rainbow vent fluids (36°14'N, MAR): the influence of ultramafic rocks and phase separation on trace metal content in Mid-Atlantic Ridge hydrothermal fluids. Chem. Geol. 184, 37–48.

El-Rahman, Y.A., Gutzmer, J., Li, X.H., Seifert, T., Li, C.F., Ling, X.X., Li, J., 2019. Not all Neoproterozoic iron formations are glaciogenic: Sturtian-aged non-Rapitan exhalative iron formations from the Arabian–Nubian Shield. Miner. Deposita 55, 577–596.

Feng, L., Huang, J., Lu, D., Zhang, Q., 2017. Major and trace element geochemistry of the Neoproterozoic syn-glacial Fulu iron formation, South China. Geol. Mag. 154 (6), 1371–1380.

Fonte-Boa, T.M.R., Novo, T.A., Pedrosa-Soares, A.C., Dussin, I., 2017. Records of Mesoproterozoic taphrogenic events in the eastern basement of the Araçuaí Orogen, southeast Brazil. Braz. J. Geol. 47 (3), 447–466.

Frimmel, H.E., Tack, L., Basei, M., Nutman, A.P., Boven, A., 2006. Provenance and chemostratigraphy of the Neoproterozoic west Congolian group in the Democratic republic of Congo. J. Afr. Earth Sci. 46, 221–239.

Gaucher, C., Sial, A.N., Frei, R., 2015. Chemostratigraphy of Neoproterozoic banded iron formation (BIF): types, age and origin. In: Ramkumar, M. (Ed.), Chemostratigraphy: Concepts, Techniques, and Applications. Elsevier, pp. 433–449 (Chapter 17).

Gomes, S.D., Figueiredo e Silva, R.C., Kemp, A.I.S., Santos, J.O.S., Hagemann, S.G., Lobato, L.M., Rosière, C.A., Novo, T.A., 2020. Zircon U–Pb ages and Hf isotope compositions of Açucena granite (Borrachudos suite): implications for statherian-Cambrian tectonomagmatic evolution of the southern border of the São Francisco craton, Brazil. J. S. Am. Earth Sci. 100, 102543.

Gravenor, C.P., Von Brunn, V., Dreimanis, A., 1984. Nature and classification of waterlain glaciogenic sediments, exemplified by Pleistocene, Late Paleozoic and Late Precambrian deposits. Earth Sci. Rev. 20, 105–166.

Gross, G.A., 1980. A classification of iron formations based on depositional environments. Can. Mineral. 18, 215–222.

Guadagnin, F., Chemale, F., 2015. Detrital zircon record of the Paleoproterozoic to mesoproterozoic cratonic basins in the São Francisco craton. J. S. Am. Earth Sci. 60, 104–116.

Halverson, G.P., Poitrasson, F., Hoffman, P.F., Nedelec, A., Montel, J.-M., Kirby, J., 2011. Fe isotope and trace element geochemistry of the Neoproterozoic syn-glacial Rapitan iron formation. Earth Planet Sci. Lett. 309, 100–112.

Hoffman, P.F., Kaufman, A.J., Halverson, G.P., Schrag, D.P., 1998. A Neoproterozoic snowball earth. Science 281, 1342–1346.

Hu, J., Wang, H., Zhang, L., 2020. A rare earth element and Nd isotopic investigation into the provenance and deposition of the Dahongliutan banded iron formation and associated carbonates, NW China: implications on Neoproterozoic seawater compositions. Precambrian Res. 342, 105685.

Ilyin, A.V., 2009. Neoproterozoic banded iron formations. Lithol. Miner. Resour. 44 (1), 78–86.

Isotta, C.A.L., Rocha-Campos, A.C., Yoshida, R., 1969. Striated pavement of the Upper-Precambrian glaciation in Brazil. Nature 222, 466–468.

James, H.L., 1954. Sedimentary facies of iron-formation. Econ. Geol. 49, 235–293.

Karfunkel, J., Hoppe, A., 1988. Late Proterozoic glaciation in central-eastern Brazil: synthesis and model. Palaeogeogr. Palaeoclimatol. Palaeoecol. 65, 1–21.

Kirschvink, J.L., 1992. Late Proterozoic low-latitude global glaciation: the snowball earth. In: Schopf, J.W., Klein, C. (Eds.), The Proterozoic Biosphere. Cambridge University Press, Cambridge, pp. 51–52.

Klein, C., 2005. Some Precambrian banded iron-formations (BIFs) from around the world: their age, geologic setting, mineralogy, metamorphism, geochemistry, and origin. Am. Mineral. 90, 1473–1499.

Klein, C., Beukes, N.J., 1993. Sedimentology and geochemistry of the glaciogenic late Proterozoic rapitan iron-formation in Canada. Econ. Geol. 88, 542–565.

Klein, C., Ladeira, E.A., 2004. Geochemistry and mineralogy of Neoproterozoic banded iron-formations and some selected, siliceous manganese formations from Urucum District, Mato Grosso do Sul, Brazil. Econ. Geol. 99, 1233–1244.

Kuchenbecker, M., Pedrosa-Soares, A.C., Babinski, M., Fanning, M., 2015. Detrital zircon age patterns and provenance assessment for pre-glacial successions of the Neoproterozoic Macaúbas Group, Araçuaí orogeny, Brazil. Precambrian Res. 266, 12–26.

Lechte, M., Wallace, M., 2016. Sub-ice shelf ironstone deposition during Neoproterozoic Sturtian glaciation. Geology 44 (11), 891–894.

Lechte, M.A., Wallace, M.W., Hood, A.S., Planavsky, N., 2018a. Cryogenian iron formations in the glaciogenic Kingston Peak Formation, California. Precambrian Res. 310, 443–462.

Lechte, M.A., Wallace, M.W., Hoffmann, K.H., 2018b. Glacio-marine iron formation deposition in a c. 700 Ma glaciated margin: insights from the Chuos Formation, Namibia. In: Le Heron, D.P., Hogan, K.A., Phillips, E.R., Huuse, M., Busfield, M.E., Graham, A.G.C. (Eds.), Glaciated Margins: the Sedimentary and Geophysical Archive, vol. 475. Geological Society, London, Special Publications, pp. 9–34.

Lombello, J.C., 2020. Geologia e recursos minerais das folhas Nova Aurora (SD.23-Z-D-V-4), Rio Pardo de Minas (SD.23-Z-D-V-2) e Santo Antônio do Retiro (SD.23-Z-D-II-4): projeto Rio Pardo de Minas, escala 1:50.000, estado de Minas Gerais. J.C. Lombello (org.) - Belo Horizonte: CPRM, p. 139, 2020.

Lottermoser, B.G., Ashley, P.M., 2000. Geochemistry, petrology and origin of Neoproterozoic ironstones in the eastern part of the Adelaide Geosyncline, South Australia. Precambrian Res. 101, 49–67.

Ludwig, K.R., 2003. User's Manual for Isoplot/Ex Version 3.0. A Geochronological Toolkit for Microsoft Excel. Berkeley Geochronological Center, Special Publication No. 4, Berkeley, USA, p. 74.

Machado, N., Schrank, A., Abreu, F.R., ALmeida-Abreu, P.A., 1989. Resultados preliminares da geocronologia U-Pb na Serra do Espinhaço Meridional. Boletim do Núcleo Minas Gerais-Sociedade Brasileira de Geologia 10, 171–174.

Magalhães, J.R., Pedrosa-Soares, A., Dussin, I., Müntener, O., Pinheiro, M.P.P., Silva, L. C., Knauer, L.G., Bouvier, A., Baumgartner, L., 2018. First Lu-Hf, $\delta^{18}O$ and trace elements in zircon signatures from the Statherian Espinhaço anorogenic province (Eastern Brazil): geotectonic implications of a silicic large igneous province. Braz. J. Geol. 48 (4), 735–759.

Mario, A.F.G., 2015. Caracterização geofísica e geológica das formações ferríferas do Grupo Macaúbas – MG. PhD Dissertation. Instituto de Geociências e Ciências Exatas do Campus de Rio Claro, UNESP, p. 315.

Marshak, S., Alkmim, F.F., Whittington, A., Pedrosa-Soares, A.C., 2006. Extensional collapse in the Neoproterozoic Araçuaí orogen, eastern Brazil: a setting for reactivation of asymmetric crenulation cleavage. J. Struct. Geol. 28, 129–147.

McGee, B., Babinski, M., Trindade, R., Collins, A.S., 2018. Tracing final Gondwana assembly: age and provenance of key stratigraphic units in the southern Paraguay Belt, Brazil. Precambrian Res. 307, 1–33.

Menezes, R.C.L., Conceição, H., Rosa, M.L.S., Macambira, M.J.B., Galarza, M.A., Rios, D. C., 2012. Geoquímica e geocronologia de granitos anorogenicos tonianos (c. 914–899 Ma) da Faixa Araçuaí no Sul do Estado da Bahia. Geonomos 20, 1–13.

Moraes, L.J., Guimarães, D., 1931. The diamond-bearing region of northern minas Gerais, Brazil. Econ. Geol. 26, 502–530.

Moreira, H.F., 2017. Caracterização petrológica, geoquímica e geocronológica de corpos intrusivos máficos da porção central da Serra do Espinhaço. Master Thesis. Departamento de Geologia, UFOP, p. 176.

Moreira, H.F., Danderfer, A., Costa, A.F.O., Bersan, S.M., Lana, C.C., Queiroga, G.N., 2020. Record of Early Tonian mafic magmatism in the central Espinhaço (Brazil): new insights for break-up of the Neoproterozoic landmass ancestor of São Francisco-Congo paleocontinent. Geoscience Frontiers 11 (6), 2323–2347.

Mourão, M.A.A., Grossi-Sad, J.H., 1997. Geologia da Folha Padre Carvalho. In: Grossi-Sad, J.H., Lobato, L.M., Pedrosa-Soares, A.C., Soares-Filho, B.S. (Eds.), Projeto Espinhaço, Belo Horizonte, pp. 380–428. CODEMIG.

Noce, C.M., Pedrosa-Soares, A.C., Grossi-Sad, J.H., Baars, F.J., Guimarães, M.L.V., Mourão, M.A.A., Oliveira, M.J.R., Roque, N.C., 1997. Nova divisão estratigráfica regional do Grupo Macaúbas na Faixa Araçuaí: O registro de uma bacia neoproterozoica. Boletim do Núcleo Minas Gerais - Sociedade Brasileira de Geologia 14, 29–31.

Pacheco, F.E.R.C., Caxito, F.A., Pedrosa-Soares, A.C., Dussin, I.A., Gonçalves-Dias, T., 2021. Detrital zircon U-Pb and Lu-Hf data for a kinzigitic gneiss (Jequitinhonha Complex, Araçuaí Orogen, SE Brazil) constrain the age of a huge storage of Ediacaran carbon. J. S. Am. Earth Sci. 105, 102709.

Pecoits, E., Gingras, M., Aubet, N., Konhauser, M., 2008. Ediacaran in Uruguay: palaeoclimatic and palaeobiological implications. Sedimentology 55, 689–719.

Pedrosa-Soares, A.C., 1995. Potencial aurífero do Vale do Araçuaí, Minas Gerais: história da exploração e controle tectonometamórfico. PhD Dissertation. Instituto de Geociências, Universidade de Brasília, p. 177.

Pedrosa-Soares, A.C., Alkmim, F.F., 2011. How many rifting events preceded the development of the Araçuaí-West Congo orogen? Geonomos 19, 244–251.

Pedrosa-Soares, A.C., Noce, C.M., Vidal, P., Monteiro, R.L.B.P., Leonardos, O.H., 1992. Towards a new tectonic model for the late Proterozoic Araçuaí (SE Brazil)-West Congolian (SW African) belt. J. S. Am. Earth Sci. 6 (1/2), 33–47.

Pedrosa-Soares, A.C., Vidal, P., Leonardos, O.H., Brito-Neves, B.B., 1998. Neoproterozoic oceanic remnants in eastern Brazil: further evidence and refutation of an exclusively ensialic evolution for the Araçuaí- West Congo Orogen. Geology 26, 519–522.

Pedrosa-Soares, A.C., Babinski, M., Noce, C., Martins, M., Queiroga, G., Vilela, F., 2011a. The Neoproterozoic Macaúbas group (Araçuaí orogen, SE Brazil). In: Arnaud, E., Halverson, G.P., Shields-Zhou, G. (Eds.), The Geological Record of Neoproterozoic Glaciations, vol. 36. Geological Society of London, Memoirs, pp. 523–534.

Pedrosa-Soares, A.C., Cordani, U.G., Nutman, A., 2000. Constraining the age of Neoproterozoic glaciation in Eastern Brazil: first U-Pb (SHRIMP) data of detrital zircons. Rev. Bras. Geociencias 30 (1), 58–61.

Pedrosa-Soares, A.C., Noce, C.M., Wiedemann, C., Pinto, C.P., 2001. The Araçuaí-West-Congo Orogen in Brazil: an overview of a confined orogen formed during Gondwanaland assembly. Precambrian Res. 110 (1–4), 307–323.

Pedrosa–Soares, A.C., Alkmim, F.F., Tack, L., Noce, C.M., Babinski, M., Silva, L.C., Martins–Neto, M.A., 2008. Similarities and differences between the Brazilian and African counterparts of the Neoproterozoic Araçuaí–west Congo orogen. In: Pankhurst, R.J., Trouw, R.A.J., de Brito Neves, B.B., De Wit, M.J. (Eds.), West Gondwana: Pre–cenozoic Correlations across the South Atlantic Region, vol. 294. Geological Society, London, Special Publications, pp. 153–172.

Pedrosa–Soares, A.C., De Campos, C., Noce, C.M., Silva, L.C., Novo, T., Roncato, J., Medeiros, S., Castañeda, C., Queiroga, G., Dantas, E., Dussin, I., Alkmim, F.F., 2011b. Late Neoproterozoic–Cambrian granitic magmatism in the Araçuaí orogen (Brazil), the eastern Brazilian Pegmatite province and related mineral resources. Geological Society, London, Special Publications 350, 25–51.

Pedrosa-Soares, A.C., Dussin, I.A., Nseka-Mbemba, P., Baudet, D., Alonso, M.F., Tack, Luc, 2016. Tonian rifting events on the Congo-São Francisco palaeocontinent: new evidence from U-Pb and Lu-Hf data from the Shinkakasa plutonic complex (Boma region, West Congo Belt, Democratic Republic of Congo). In: 5th International Geologica Belgica Meeting, Mons, Belgic, Abstract Book, p. 44.

Pedrosa-Soares, A.C., Deluca, C., Araujo, A., Gradim, C., Lana, C., Dussin, I., Silva, L.C., Babinski, M., 2020. O Orógeno Araçuaí à luz da geocronologia U-Pb: um tributo a Umberto Cordani. In: Bartorelli, A., Teixeira, W., Brito-Neves, B.B. (Eds.), Geocronologia e evolução tectônica do Continente Sul-Americano: a contribuição de Umberto Cordani. Solaris Edições Culturais, São Paulo, Brazil, first ed., pp. 250–272.

Peixoto, E., Pedrosa-Soares, A.C., Alkmim, F.F., Dussin, I.A., 2015. A suture-related accretionary wedge formed in the Neoproterozoic Araçuaí orogen (SE Brazil) during Western Gondwanaland assembly. Gondwana Res. 27, 878–896.

Peixoto, E., Alkmim, F.F., Pedrosa-Soares, A.C., 2018a. The Rio Pardo salient, northern Araçuaí orogen: an example of a complex basin-controlled fold-thrust belt curve. Braz. J. Geol. 48, 25–49.

Peixoto, E., Alkmim, F.F., Pedrosa-Soares, A., Lana, C., Chaves, A.O., 2018b. Metamorphic record of collision and collapse in the Ediacaran-Cambrian Araçuaí orogen, SE-Brazil: insights from P-T pseudosections and monazite dating. J. Metamorph. Geol. 36, 147–172.

Piacentini, T., Boggiani, P.C., Yamamoto, J.K., Freitas, B.V., Campanha, G.A.C., 2007. Formação ferrífera associada à sedimentação glaciogênica da Formação Puga (Marinoano) na Serra da Bodoquena, MS. Rev. Bras. Geociencias 37 (3), 530–541.

Pinto, C.P., Silva, M.A., 2014. Companhia de Desenvolvimento Econômico de Minas Gerais, CODEMIG e Serviço Geológico do Brasil. Mapa Geológico do Estado de Minas Gerais, Escala 1:1.000.000, CPRM.

Planavsky, N., Bekker, A., Rouxel, O.J., Kamber, B., Hofmann, A., Knudsen, A., Lyons, T. W., 2010. Rare earth element and yttrium compositions of Archean and Paleoproterozoic Fe formations revisited: new perspectives on the significance and mechanisms of deposition. Geochem. Cosmochim. Acta 74 (22), 6387–6405.

Queiroga, G.N., 2006. A seção sedimentar sulfetada do ofiolito de Ribeirão da Folha e seu potencial metalogenético, Orógeno Araçuaí, MG. Master Thesis. Instituto de Geociências, Universidade Federal de Minas Gerais, Belo Horizonte, p. 107.

Queiroga, G.N., 2010. Caracterização de restos de litosfera oceânica do Orógeno Araçuaí entre os paralelos 17° e 21° S. PhD Dissertation. Instituto de Geociências, Universidade Federal de Minas Gerais, Belo Horizonte, p. 180.

Queiroga, G.N., Dussin, I.A., Martins, M., Machado, M.C., Kawashita, K., Chemale, F., 2012. Roteiro de Campo – Rochas Ígneas. Geologia Estrutural e Estratigrafia do Sistema Espinhaço – Chapada Diamantina e sua Aplicação nas Bacias Mesocenozóicas da Margem Passiva Brasileira. FUNDEP/PETROBRÁS, Belo Horizonte, pp. 170–195.

Queiroga, G.N., Pedrosa-Soares, A.C., Noce, C.M., Alkmim, F.F., Pimentel, M.M., Dantas, E., Martins, M., Castañeda, C., Suita, M.T.F., Prichard, R., 2007. Age of the Ribeirão da Folha ophiolite, Araçuaí Orogen: the U-Pb zircon (LA-ICPMS) dating of a plagiogranite. Geonomos 15 (1), 61–65.

Rocha-Campos, A.C., Hasui, Y., 1981. Tillites of the Macaúbas group (Proterozoic) in central minas Gerais and southern Bahia, Brazil. In: Hambrey, M.J., Harland, W.B. (Eds.), Earth's Pre-pleistocene Glacial Record. Cambridge University Press, pp. 933–939.

Rolim, V.K., Rosière, C.A., Santos, J.O.S., McNaughton, N.J., 2016. The Orosirian-Statherian banded iron formation-bearing sequences of the southern border of the Espinhaço range, southeast Brazil. J. S. Am. Earth Sci. 65, 43–66.

Rooney, A.D., Strauss, J.V., Brandon, A.D., Macdonald, F.A., 2015. A Cryogenian chronology: two long-lasting synchronous Neoproterozoic glaciations. Geology 43, 459–462.

Roque, N.C., Grossi-Sad, J.H., Noce, C.M., Fonseca, E., 1997. Geologia da Folha Rio Pardo de Minas. In: Grossi-Sad, J.H., Lobato, L.M., Pedrosa-Soares, A.C., Soares-Filho, B.S. (Eds.), Projeto Espinhaço Em CD-ROM. Belo Horizonte, CODEMIG, pp. 125–221.

Rosa, M.L.S., Conceição, H., Macambira, M.J., Galarza, M.A., Cunha, M.P., Menezes, R.C. L., Marinho, M.M., Cruz-Filho, B.E., Rios, D.C., 2007. Neoproterozoic anorogenic magmatism in the Southern Bahia Alkaline Province of NE Brazil: U–Pb and Pb–Pb ages of the blue sodalite syenites. Lithos 97, 88–97.

Rosière, C.A., Bekker, A., Rolim, V.K., Santos, J.O.S., 2019. Post-great oxidation event Orosirian-statherian iron formations on the São Francisco craton: geotectonic implications. Isl. Arc 28 (4), e12300. https://doi.org/10.1111/iar.12300.

Schannor, M., Lana, C., Fonseca, M.A., 2019. São Francisco-Congo Craton break-up delimited by U–Pb–Hf isotopes and trace elements of zircon from metasediments of the Araçuaí Belt. Geoscience Frontiers 10, 611–628.

Schannor, M., Lana, C., Mazoz, A., Narduzzi, F., Cutts, K., Fonseca, M., 2020. Paleoproterozoic sources for Cordilleran-type Neoproterozoic granitoids from the Araçuaí orogen (SE Brazil): constraints from Hf isotope zircon composition. Lithos 378–379, 105815.

Schobbenhaus, C., 1972. Estudo geoeconômico preliminar do depósito de ferro do Rio Peixe Bravo, Norte de Minas Gerais. In: Série Geologia Econômica, vol. 8. Divisão de Geologia, Superintendência do Desenvolvimento do Nordeste - SUDENE, Recife, p. 36.

Silva, L.C., Pedrosa-Soares, A.C., Teixeira, L., Armstrong, R., 2008. Tonian rift-related, A-type continental plutonism in the Araçuaí Orogen, eastern Brazil: new evidence for the breakup stage of the São Francisco Congo Paleocontinent. Gondwana Res. 13, 527–537.

Silva, L.C., Pedrosa-Soares, A.C., Armstrong, R., Pinto, C.P., Magalhães, J.T.R., Pinheiro, M.A.P., Santos, G.G., 2016. Disclosing the Paleoarchean to Ediacaran history of the São Francisco craton basement: the Porteirinha domain (northern Araçuaí orogen, Brazil). J. S. Am. Earth Sci. 68, 50–67.

Silveira, E.M., Söderlund, U., Oliveira, E.P., Ernst, R., Menezes Leal, A.B., 2013. First precise U-Pb baddeleyite ages of 1500 Ma mafic dykes from the São Francisco Craton, Brazil, and tectonic implications. Lithos 174, 144–156.

Silveira Braga, F.C., Rosière, C.A., Queiroga, G.N., Rolim, V.K., Santos, J.O.S., McNaughton, N.J., 2015. The statherian itabirite-bearing sequence from the morro Escuro ridge, santa maria de Itabira, minas Gerais, Brazil. J. S. Am. Earth Sci. 58, 33–53.

Smith, A.J.B., 2018. The iron formations of southern Africa. In: Siegesmund, S., Basei, M., Oyhantçabal, P., Oriolo, S. (Eds.), Geology of Southwest Gondwana. Springer, pp. 469–491 (Chapter 17).

Söderlund, U., Patchett, P.J., Vervoot, J.D., Isachsen, C.E., 2004. The ^{176}Lu decay constant determined by Lu-Hf and U-Pb isotope systematic of Precambrian mafic intrusions. Earth Planet Sci. Lett. 219 (3–4), 311–324.

Souza, M.E.S., 2016. Caracterização litoestrutural e geocronológica dos xistos verdes e metagabros do Grupo Macaúbas na Faixa Terra Branca - Planalto de Minas, Minas Gerais. Master Thesis. Departamento de Geologia, UFOP, p. 251.

Souza, M.E.S., Martins, M.S., Queiroga, G.N., Leite, M., Oliveira, R.G., Dussin, I., Pedrosa-Soares, A.C., 2019. Paleoenvironment, sediment provenance and tectonic setting of Tonian basal deposits of the Macaúbas basin system, Araçuaí orogen, southeast Brazil. J. S. Am. Earth Sci. 96, 102393.

Straathof, G.B., 2011. Neoproterozoic Low Latitude Glaciations: an African Perspective. PhD Dissertation. University of Edinburgh, Scotland, UK.

Stern, R.J., Mukherjee, S.K., Miller, N.R., Ali, K., Johnson, P.R., 2013. ~750 Ma banded iron formation from the Arabian-Nubian Shield-Implications for understanding Neoproterozoic tectonics, volcanism, and climate change. Precambrian Res. 239, 79–94.

Swanson-Hysell, N.L., Rose, C.V., Calmet, C.C., Halverson, G.P., Hurtgen, M.T., Maloof, A.C., 2010. Cryogenian glaciation and the onset of carbon-isotope decoupling. Science 328, 608–611.

Tack, L., Wingate, M.T.D., Liégeois, J.P., Fernandez-Alonso, M., Deblond, A., 2001. Early Neoproterozoic magmatism (1000-910 Ma) of the Zadinian and mayumbian groups (Bas-Congo): onset of rodinian rifting at the western edge of the Congo craton. Precambrian. Research 110, 277–306.

Tack, L., Wingate, M.T.D., De Waele, B., Meert, J., Belousova, E., Griffin, B., Tahon, A., Fernandez-Alonso, M., 2010. The 1375 Ma Kibaran Event in Central Africa: prominent emplacement of bimodal magmatism under extensional regime. Precambrian Res. 180, 63–84.

Taylor, S., McLennan, S., 1985. The Continental Crust: its Composition and Evolution. Blackwell Scientific Publications, p. 312.

Teixeira, W., Ávila, C., Dussin, I., Correa-Neto, A., Bongiolo, E., Santos, O., Barbosa, N., 2015. A juvenile accretion episode (2.35-2.32 Ga) in the Mineiro belt and its role to the Minas accretionary orogeny: zircon U-Pb-Hf and geochemical evidences. Precambrian Res. 256, 148–169.

Thiéblemont, D., Callec, Y., Fernandez-Alonso, M., Chène, F., 2018. A geological and isotopic framework of Precambrian terrains in Western Central Africa: an introduction. In: Geology of Southwest Gondwana, Regional Geology Reviews. Springer Publ, pp. 107–132. https://doi.org/10.1007/978-3-319-68920-3_5.

Thiéblemont, D., Castaing, C., Billa, M., Bouton, A., Préat, A., 2009a. Notice explicative de la carte géologique et des ressources minérales de la République Gabonaise à 1/ 1000000. Programme Sysmin 8 ACP GA 017, Ministère des Mines, du Pétrole, des Hydrocarbures. Direction Générale des Mines et de la Géologie, p. 384.

Thiéblemont, D., Prian, J.P., Goujou, J.C., Boulingui, B., Ekogha, H., Kassadou, A.B., Simo, N.S., Walemba, A., Préat, A., Theunissen, K., Cocherie, A., Guerrot, C., 2009b. Timing and Characteristics of Neoproterozoic Magmatism in SW-Gabon. First Geochronological and Geochemical Data on the West-Congolian Orogen in Gabon SYSMIN Project, Gabon 2005–2009. 23th Colloquium African Geology (CAG23). Abstract Book and Poster, Johannesburg (South Africa), January 2009.

Trendall, A.F., 2002. The Significance of Iron-Formation in the Precambrian Stratigraphic Record, vol. 33. International Association of Sedimentologists Special Publication, pp. 33–66.

Uhlein, A., Trompette, R., Alvarenga, C., 1999. Neoproterozoic glacial and gravitational sedimentation on a continental rifted margin: the Jequitaí-Macaúbas sequence (Minas Gerais, Brazil). J. S. Am. Earth Sci. 12, 435–451.

Uhlein, A., Trompette, R., Egydio-Silva, M., 1998. Proterozoic rifting and closure, SE border of the São Francisco Craton, Brazil. J. S. Am. Earth Sci. 11, 191–230.

Urban, H., Stribrny, B., Lippolt, H.J., 1992. Iron and manganese deposits of the Urucum district, mato Grosso do Sul, Brazil. Econ. Geol. 87, 1375–1392.

Velasco, A.I., Costa, F.G., 1970. Relatório dos estudos de reconhecimento da formação ferrífera de "3 Rios" situado na região de divisa dos municípios Grão Mogol, Porteirinha e Rio Pardo do Estado de Minas Gerais. Geological Survey of Brazil, Belo Horizonte, p. 49.

Vervoot, J.D., Blichert-Toft, J., 1999. Evolution of depleted mantle: Hf isotope evidence from juvenile rocks through time. Geochem. Cosmochim. Acta 54, 1683–1697.

Vilela, O.V., 1986. As jazidas de minério de ferro dos municípios de Porteirinha, Rio Pardo de Minas, Riacho dos Machados e Grão-Mogol, norte de Minas Gerais. In: Schobbenhaus, C., Coelho, C.E.S. (Eds.), Principais Depósitos Minerais do Brasil: Ferro e Metais da Indústria do Aço, vol. 2, pp. 111–120.

Vilela, F.T., 2010. Caracterização de metadiamictitos ferruginosos da Formação Nova Aurora (Grupo Macaúbas, Orógeno Araçuaí) a oeste de Salinas, MG. Master Thesis. Instituto de Geociências, Universidade Federal de Minas Gerais, Belo Horizonte, p. 135.

Vilela, F.T., Pedrosa-Soares, A.C., Carvalho, M.T.N., Arimateia, R., Santos, E., Voll, E., 2014. Metalogênese da Faixa Araçuaí: o Distrito Ferrífero Nova Aurora (Grupo Macaúbas, Norte de Minas Gerais) no contexto dos recursos minerais do Orógeno Araçuaí. In: Silva, M.G., Rocha-Neto, M.B., Jost, H., Kuyumjian, R.M. (Eds.), Metalogênese das Províncias Tectônicas Brasileiras, first ed., pp. 415–430 CPRM (www.cprm.gov.br, Rio de Janeiro, Brazil.

Viveiros, J.F.M., Sá, E.L., Vilela, O.V., Santos, O.M., Moreira, J.M.P., Holder-Neto, F., Vieira, V.S., 1978. Geologia dos vales dos rios Peixe Bravo e Alto Vacaria, norte de Minas Gerais. In: SBG. Congresso Brasileiro Geologia, 30, Recife, vol. 1. Anais, pp. 243–254.

Voll, E., Silva, A.M., Pedrosa-Soares, A.C., 2020. Tracking iron-rich rocks beneath Cenozoic tablelands: an integration of geological, airborne geophysical and remote sensing data from northern Minas Gerais State, SE Brazil. J. S. Am. Earth Sci. 101, 102604.

Young, G.M., 1976. Iron-Formation and glaciogenic rocks of the rapitan group, Northwest territories, Canada. Precambrian Res. 3 (2), 137–158.

Young, G.M., 1988. Proterozoic plate tectonics, glaciation and iron-formations. Sediment. Geol. 58, 127–144.

Zhang, Q., Li, X., Feng, L., Huang, J., Song, B., 2008. A new age constraint on the onset of the Neoproterozoic glaciations in the Yangtze Platform, South China. J. Geol. 116, 423–429.